Carbon vacancy Mediated CH_4 Activation and Carbon-Carbon Coupling on TiC(001) Surface : A First Principles Investigation

A Thesis

submitted to
Indian Institute of Science Education and Research Pune
in partial fulfillment of the requirements for the
BS-MS Dual Degree Programme

by

Rapti Pal

Indian Institute of Science Education and Research Pune
Dr. Homi Bhabha Road,
Pashan, Pune 411008, INDIA.

April, 2023

Supervisor: Prasenjit Ghosh

Certificate

This is to certify that this dissertation entitled **Carbon vacancy Mediated CH_4 Activation and Carbon-Carbon Coupling on TiC(001) Surface : A First Principles Investigation** towards the partial fulfilment of the BS-MS dual degree programme at the Indian Institute of Science Education and Research, Pune represents study/work carried out by Rapti Pal at Indian Institute of Science Education and Research under the supervision of Prasenjit Ghosh, Associate Professor, Department of Physics , during the academic year 2022-2023.

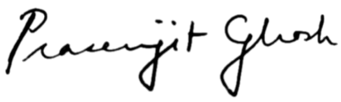

Prasenjit Ghosh

Committee:

Prasenjit Ghosh

Arun Venkatanathan

This thesis is dedicated to my parents and my brother

Declaration

I hereby declare that the matter embodied in the report entitled **Carbon vacancy Mediated CH_4 Activation and Carbon-Carbon Coupling on TiC(001) Surface : A First Principles Investigation** are the results of the work carried out by me at the Department of Physics, Indian Institute of Science Education and Research, Pune, under the supervision of Prasenjit Ghosh and the same has not been submitted elsewhere for any other degree.

Rapti Pal

Acknowledgments

I extend my sincere gratitude to my supervisor, Dr. Prasenjit Ghosh, for his unwavering support throughout this project. I am deeply appreciative of his willingness to answer every question I had, even the trivial ones, for ensuring I always had enough resources to carry out my project, and for always inspiring me to improve.

I would also like to thank my thesis advisory committee member, Dr. Arun Venkatanathan, for his valuable comments and suggestions.

I would like to express my sincere appreciation to my labmates for their insightful suggestions and for the many enriching conversations I have had with them.

I am extremely grateful to my friends for patiently listening to me and for their encouragement.

I owe my deepest gratitude to my mother, who has been my biggest inspiration and role model and whose kindness and sincerity are a constant source of motivation for me. I am thankful to my father for always ensuring my well-being, and to my brother for being my toughest critic and my biggest supporter.

Lastly, I would like to acknowledge National Supercomputing Mission (NSM) for providing computing resources of 'PARAM Brahma' at IISER Pune and 'PARAM Utkarsh' at C-DAC Bangalore, which are implemented by C-DAC and supported by the Ministry of Electronics and Information Technology (MeitY) and Department of Science and Technology (DST), Government of India. I also acknowledge the Center for Computational Materials Science, Institute for Materials Research, Tohoku University, Japan for providing computational facilities at the MASAMUNE Supercomputer.

Abstract

Methane is the main component of natural gas and one of the major greenhouse gases contributing to global warming. Therefore, capturing methane and utilizing it for chemical processes is highly desirable. Methane however, is a highly stable molecule, making methane activation a challenging process. As such finding a suitable catalyst for methane activation is one of the "holy grails" of catalysis. Catalysts that have been studied for methane activation exhibit a trade-off between activity and selectivity. On most catalysts the activation of the first C-H bond is difficult while the dissociation of the remaining C-H bonds is facile, leading to complete dissociation of methane into carbon and hydrogen. The C-deposition on the catalyst surface leads to catalyst poisoning and makes the surface unsuitable for repeated catalytic cycles. Additionally, the facile nature of the reaction poses a challenge to the direct conversion of methane into valuable products.

Transition metal carbides such as Titanium carbide (TiC) have been widely used for small molecule activation. TiC is an easily available and a very cheap material. However it rarely exists in nature in the exact stoichiometric form, and mostly contains carbon vacancies. Methane activation is however not feasible on pristine TiC surfaces. Using Density Functional Theory based calculations, we have studied methane activation on TiC(001) surfaces containing carbon vacancies to understand how the concentration of C-vacancies affects the activation of methane on TiC(001).

Dissociation of CH_4 on the single vacancy surface is found to be less facile and hence more selective compared to CH_4 dissociation on the divacancy surface. On the divacancy surface the facile nature of the reaction leads to deposition of a carbon atom in one of the two vacancies. The selectivity of CH_4 activation on the single vacancy surface is desirable and hence this surface is explored further for the formation of C_2 compounds. Acetylene or C_2H_2 formation is found to be thermodynamically and kinetically feasible on the single vacancy surface. For a catalyst to be economically viable it should be able to sustain repeated catalytic cycles. Hence, we explore the regeneration of the catalyst which involves the regeneration of the C-vacancy by the removal of H atoms in the form of H_2 molecules. Finally, we have also studied the effect of temperature on the reactivity of the surface. We observe that while C_2H_2 formation is feasible at relatively low temperatures compared to the existing catalysts, one needs to go to higher temperatures for catalyst regeneration and C_2H_2 desorption.

Contents

Abstract **xi**

1 Introduction **5**

2 Methods **9**

2.1 Time-Independent Schrodinger Equation and the Born Oppenheimer Approximation 9

2.2 Density Functional Theory 11

2.3 Surface Models 15

2.4 Zero Point Energy and Free Energy Corrections 16

2.5 Charge Analysis 19

2.6 Transition State Theory and Nudged Elastic Band calculations 20

3 Results and Discussion **25**

3.1 CH_4 molecule 25

3.2 Bulk TiC 25

3.3 TiC(001) surfaces 26

3.4 CH_4 activation on single C vacancy 27

3.5 CH_4 activation on divacancies 36

3.6 C-C coupling on single vacancy surface 46
3.7 Temperature dependence of energetics 53

4 Conclusion **55**

5 Appendix **57**

5.1 CH_3 diffusion 57
5.2 CH_2 diffusion 59
5.3 CH diffusion 61
5.4 H_2 evolution on defect-free surface 62
5.5 Temperature dependence 63

List of Figures

3.1 Bulk TiC band structure and density of states 26

3.2 TiC(001) surfaces 27

3.3 CH_4 adsorption configuration on single vacancy 28

3.4 Reaction profile for $CH_4^\star$ (S0)$\rightarrow$ $CH_3^\star$+$H^\star$(S1) on single vacancy 29

3.5 Reaction profile for $CH_3^\star$+$H^\star$ (S1) $\rightarrow$ $CH_2^\star$+2$H^\star$ (S2) on single vacancy . . . 31

3.6 Reaction profile for $CH_2^\star$+2$H^\star$ (S2) $\rightarrow$ $CH^\star$+3$H^\star$ (S3) on single vacancy . . 32

3.7 Reaction profile for $CH^\star$+3$H^\star$ (S3) $\rightarrow$ $C^\star$+4$H^\star$ (S4) on single vacancy 33

3.8 Complete Reaction Profile for $CH_4^\star$ $\rightarrow$ $C^\star$+4$H^\star$ 33

3.9 Projected Density of States (PDOS) and Integrated Local DOS for CH_4 adsorbed on the single vacancy. 34

3.10 Charge transfer isosurface for CH_4 adsorption on single vacancy 35

3.11 Adsorption of CH_4 on surface with divacancy (D0) 37

3.12 Reaction profile for $CH_4^\star$ (D0) $\rightarrow$ $CH_3^\star$+$H^\star$ (D1) on surface with divacancy. 38

3.13 Reaction profile for $CH_3^\star$+$H^\star$ (D1) $\rightarrow$ $CH_2^\star$+2$H^\star$ (D2) on surface with divacancy 39

3.14 Reaction profile for $CH_2^\star$+2$H^\star$ (D2) $\rightarrow$ $CH^\star$+3$H^\star$ (D3) on surface with divacancy 40

3.15 Reaction profile for $CH^\star$+3$H^\star$ (D3) $\rightarrow$ $C^\star$+4$H^\star$ (D4) on surface with divacancy 41

3.16 Complete Reaction profile for $CH_4^\star$ $\rightarrow$ $C^\star$+4$H^\star$ on surface with divacancy . 42

3.17 Projected Density of States (PDOS) and Integrated Local DOS for CH_4 adsorbed on the divacancy. 43

3.18 Charge transfer isosurfaces for CH_4 adsorption on di-vacancies 44

3.19 Schematic for C_2 coupling 47

3.20 Reaction profile for $C_2H_2^\star$ formation on the defect-free surface 49

3.21 H_2 formation at vacancy 50

3.22 $H^\star$ migration near vacancy 51

3.23 $H^\star$ migration on defect-free surface 51

3.24 H atom reoccupying the vacancy 52

3.25 H_2 evolution at the vacancy after vacancy reoccupation 52

5.1 $CH_3^\star$ migration near vacancy. 58

5.2 $CH_3^\star$ migration on defect-free surface. 58

5.3 $CH_2^\star$ migration near vacancy. 60

5.4 $CH_2^\star$ migration on defect-free surface. 60

5.5 $CH^\star$ migration near the vacancy 61

5.6 $CH^\star$ migration on the defect-free surface 62

5.7 H_2 evolution on defect-free surface. 63

List of Tables

3.1 Net Atomic Charges on the C of the $CH_x^\star$(x=0-4) 36

3.2 Net Atomic Charges on the C of the $CH_x^\star$(x=0-4) 44

3.3 Comparison of the energy barriers of CH_x (x= 1–4) cleavage. 45

3.4 Comparison of migration vs dissociation barriers for CH_x. 48

5.1 Free energies of activation of C-H bond with respect to temperature. 63

5.2 Reaction free energy (in eV) for C-H bond dissociation with respect to temperature. 64

5.3 Gibbs free energies of intermediates with respect to temperature 64

5.4 Free energy barriers for C-H bond dissociation with respect to temperature. . 65

5.5 Reaction free energy for C-H bond dissociation with respect to temperature. 65

5.6 Activation barrier and reaction Energies for CH migration on near the vacancy with respect to temperature. 66

5.7 Free energy of activation for CH migration on defect-free surface with respect to temperature. 66

5.8 Free energy of intermediate for CH migration on defect-free surface with respect to temperature. 67

5.9 Free energy for C_2H_2 formation and desorption with respect to temperature. 67

5.10 Free energy of activation for C_2H_2 formation with respect to temperature. . . 68

5.11 Reaction free energy and activation energy for H diffusion near vacancy with respect to temperature. 68

5.12 Activation energy for H diffusion on pristine surface with respect to temperature. 69

5.13 Reaction free energy and activation energy for H diffusion near vacancy with respect to temperature. 69

5.14 Reaction free energy and activation energy for H_2 evolution at the vacancy after vacancy reoccupation with respect to temperature. 70

5.15 Reaction free energy and activation energy for H_2 evolution at the vacancy after vacancy reoccupation with respect to temperature. 70

Chapter 1

Introduction

With dwindling petroleum reserves, an ever growing population and an increasing threat of global warming, alternative and clean sources of energy are the need of the hour. Methane (CH_4) is the major component of natural gas and it is a clean fossil fuel. Methane is also one of the major contributors to global warming, having a greenhouse capacity that is approximately 23 times higher than that of carbon dioxide.[1] The wide availability of methane, and the threat that free CH_4 gas poses to the atmosphere makes methane capture and utilisation the need of the hour. Synthetic routes for methane capture and utilisation via Fischer-Tropsch process involve converting it into syngas and consequently into other valuable chemicals such as olefins, gasoline and diesel. However, this involves the initial oxidation of CH_4 into CO and subsequent removal of O from CO using H_2 to form hydrocarbons. This uses up valuable H_2 that finds use in fuel cells, as well as leads to the overoxidation of CO to form CO_2.[2] The synthesis of syngas requires high-temperature, high-pressure and is an endothermic process.[3] A more economically viable alternative is the direct conversion of methane into hydrocarbons.

Methane however, is a highly stable molecule. CH_4 has four high energy C-H bonds, which along with the non-polarity of the molecule, makes it an extremely stable compound. Methane also has a low lying highest occupied molecular orbital (HOMO) and a high energy lowest unoccupied molecular orbital (LUMO) which make it non-reactive and inert.

Several outcomes of methane activation can be explored - complete removal of the C-H bonds from methane to form elemental carbon and hydrogen gas for use in fuel cells,

oxidation of methane into methanol, and the coupling of methane fragments to form C-C bonds in higher unsaturated or aromatic hydrocarbons.[4]

Methane activation has been previously explored on surfaces of metals, metal oxides,[5] transition metal carbides[6,7] and metal supported nanoparticles.[8] On these catalysts the first activation energy of methane is high, but the subsequent C-H bond dissociation steps have low activation barriers which leads to the methyl radical formed after the first activation step to form elemental carbon on the catalyst surface. This poisons the catalyst surface and reduces its reactivity.[9] The facile nature of the reaction also leads to loss of specificity and selectivity of the activation process. As a result it is desirable to find catalysts which are able to selectively activate methane under feasible conditions, and simultaneously aid in the direct conversion of methane into useful chemicals.

Late transition metals such as Ni, Pt, Pd which are commonly used catalysts for small molecule activation do not perform well with respect to methane adsorption.[10] Metal oxide surfaces such as MgO, and aluminium oxides and oxide anions have been successfully used for methane activation and oxidative coupling of methane to form ethylene.[2] Single atoms deposited on metal oxide surfaces have also exhibited increased activity towards CH_4 activation.[11] $Fe@SiO_2$ has been shown to catalyse the conversion of methane to ethylene.[12] Rh nanoparticles deposited on IrO_2 surface catalyses the conversion of methane into methanol.[13] Ni nanoparticles deposited on TiC(001) surfaces have been shown to activate CH_4 with their catalytic activity varying with their sizes.[8]

Transition metal carbides (TMCs) have been explored in the context of methane activation. Methane activation and C-C coupling has been explored on Ti_2C,[9] Mo_2C[6] and WC[7] surfaces. Ni nanoparticles deposited on TMC surfaces have been shown to activate CH_4 at room temperature.[8] However the process of depositing nanoclusters on surfaces is challenging. Additionally, these clusters are mobile on the support surface and can aggregate to form large clusters which resemble monolayers which may not very effective for catalysis. CH_4 has very low adsorption energies on pristine surfaces of TMCs such as VC, TiC, TaC making these catalysts unsuitable for methane activation.[14] Non-stoichiometric TMCs such as Mo_2C[6] and Ti_2C[9] have been shown to exhibit low activation barriers for the dissociation of the first C-H bond. Figueras et.al. have studied $MoC_x (0.5 < x < 1.1)$ nanoparticles supported on Au surface and they observe that the C concentration in the TMC nanoparticle affects the activation of CH_4.[15] In another study carried out with respect to the water gas splitting

reaction, the activities of the TiC(001) surface, and the Ti_8C_{12} and $Ti_{14}C_{13}$ nanoparticles were compared. Among the three catalysts, the C-deficient $Ti_{14}C_{13}$ nanoparticle with a C:Ti ratio of 0.928 shows the highest reactivity for water gas splitting.[16] These observations suggest that the concentration of carbon vacancies might play a role in the reactivity of metal carbide surfaces.

TiC is an early transition metal carbide with a face-centered cubic, NaCl type structure.[17] The pristine TiC(001) surface exhibits a very low adsorption energy for methane adsorption and is unsuitable for methane activation.[8] Ti_2C surfaces (which contain an excess on C vacancies) however show high reaction energies and low barriers for first C-H bond dissociation of the methane molecule but the remaining bond dissociation steps are associated with exothermic reaction energies and low activation barriers, leading to overall low selectivity of the surface, and ultimately surface poisoning due to formation of elemental C on the surface.[9] TiC rarely exists as a purely stoichiometric compound. It is prone to the formation of carbon vacancies under both Ti-rich and C-rich experimental conditions.[18]It has also been observed that carbon vacancies show a preference for segregation on the surface in bulk TiC_x, for small values of x.[17] Since catalysis is a surface phenomena, the presence of vacancies on the surface can modulate the reactivity of the surface. Therefore it could be useful to look into methane activation on TiC surfaces with carbon vacancies to understand how vacancy concentration could affect the reactivity of the species towards methane activation, and if the facile C-H bond breaking of the subsequent activated species can be arrested. In the first part of this study, we compare CH_4 activation at TiC(001) surfaces with C:Ti ratios of 0.875 and 0.75, which correspond to the presence of 12.5% and 25% C vacancies on the surface, respectively.

Among the various valuable chemicals that could be obtained from CH_4 are the C_2 products, characterized by C-C bonds, a term generally used to refer to C_2H_6, C_2H_4 and C_2H_2. There are two common routes for C-C coupling - oxidative coupling of methane (OCM) and non-oxidative coupling of methane (NOCM). OCM has some drawbacks such as the overoxidation of the C_2 products to form CO_2, and low selectivity.[19] NOCM is preferred over OCM since no oxidizing agents are required, and H_2, which is an useful fuel, can be obtained as one of the side products.[19] Some catalysts that have been able to catalyse NOCM include Pt nanoparticles deposited on CeO surfaces,[20] and Pt nanolayers.[21] On these catalysts the C-C coupling is attained at high temperatures and pressures. C_2H_2 formation has also been explored on metal carbide surfaces, such as Mo_2C,[6] WC[7] and Ti_2C.[9]

In the second part of this study, we choose the single vacancy to study the NOCM. Since CH_4 dissociation is not facile on this surface, we expect this surface to exhibit some selectivity towards the formation of C_2 species as opposed to carbon deposition on the surface (which is the more probable outcome on the surface containing divacancies). We explore the formation of acetylene or ethyne, C_2H_2. Acetylene is a useful chemical feedstock - it can be converted to various other compounds such as benzene, ethanol, can be polymerized to obtain polyacetylene, can be dimerized to obtain vinylacetylene, can be used as a dienophile in Diels Alder cyclization reactions and can be functionalized to obtain tetrachloroethane and similar compounds.[22] These compounds derived from acetylene could in turn be used in paints, pharmaceuticals, automobile fuel, plastics and so on. As a result it is desirable to explore the direct conversion of methane into acetylene on a relatively cheaply available catalyst such as TiC.

This thesis is organized into three chapters as follows. Chapter 2 outlines the methods employed for performing the first principle calculations and the techniques used for analysis. Chapter 3 elaborates on the mechanisms of methane activation on the single vacancy and di-vacancy containing TiC(001) surfaces, C_2H_2 formation on the TiC(001) surface with a single carbon vacancy and catalyst regeneration. Chapter 4 provides a conclusive outlook on the study's findings. Finally, Chapter 5 (Appendix) includes additional details that have been excluded from Chapter 3 for the sake of brevity.

Chapter 2

Methods

2.1 Time-Independent Schrodinger Equation and the Born Oppenheimer Approximation

The time-independent Schrodinger equation can be solved to obtain all the information about the stationary state electronic structure of a system of particles. The time-independent Schrodinger equation can be written as follows[23]

$$\hat{H}\Psi(\mathbf{r}) = \left[-\sum_{i=1}^{N} \frac{\hbar^2}{2M_i}\nabla_i^2 - \sum_{i=1}^{n} \frac{\hbar^2}{2m_i}\nabla_i^2 + \sum_{i<j}^{n} \frac{e^2}{r_{ij}} + \sum_{i<j}^{N} \frac{Z_i Z_j}{R_{ij}} - \sum_{i=1}^{N}\sum_{j=1}^{n} \frac{Z_i e^2}{|R_i - r_j|} \right] \Psi(\mathbf{r}) = E\Psi(\mathbf{r}) \tag{2.1}$$

where the wave function $\Psi(\mathbf{r})$ is time-independent. $\hat{H}$ is the Hamiltonian operator, which determines the total energy of the system. E represents the energy of the stationary state, and $T_N = -\sum_{i=1}^{N} \frac{\hbar^2}{2M_i}\nabla_i^2$ is the kinetic energy operator for the N nuclei, and $T_e = -\sum_{i=1}^{N} \frac{\hbar^2}{2m_i}\nabla_i^2$ is the kinetic energy of the n electrons, $V_{ee}(r) = \sum_{i<j}^{n} \frac{e^2}{r_{ij}}$ is the electron-electron interaction, $V_{NN}(R) = \sum_{i<j}^{N} \frac{Z_i Z_j}{R_{ij}}$ is the internuclear interaction and $V_{eN}(r, R) = \sum_{i=1}^{N}\sum_{j=1}^{n} \frac{Z_i e^2}{|R_i - r_j|}$ is the electron-nucleus attraction term. $R(M)$ represents the nuclear coordinates (mass) and r (m) represents the electronic coordinates (mass) respectively.

The Born-Oppenheimer approximation[24] allows one to separate the motion of the nuclei from the motion of the electrons. It is assumed that the solution to the time-independent

electronic Schrodinger equation ($\Psi_e(r, R)$) is known for a fixed arrangement of the nuclei R. This is the clamped-nuclei approximation.

$$\hat{H}_e(R) \left|\Psi_e(r; R)\right\rangle = E_e(R) \left|\Psi_e(r; R)\right\rangle \tag{2.2}$$

where H_e is the electronic Hamiltonian, written as,

$$H_e(R) = -\sum_{i=1} \frac{\hbar^2}{2m_i} \nabla_i^2 + V_{NN}(R) + V_{ee}(r) + V_{eN}(r, R) \tag{2.3}$$

where $V_{NN}(R)$ is constant for a given arrangement of nuclei denoted by R and $V_{eN}(r, R)$ depends parametrically on R.

The total wavefunction can then be expanded as

$$\Psi(r, R) = \sum_i \Psi_e^i(r, R)\Psi_N^i(R) \tag{2.4}$$

where $\Psi_e(r, R)$ is the electronic wavefunction which is a function the electronic coordinates and depends parametrically on the nuclear coordinates. $\Psi_N(R)$ is the nuclear wavefunction which depends only on the nuclear coordinates.

According to the Born-Oppenheimer approximation the nuclei move on an effective potential that is obtained by solving the electronic Schrodinger equation. Since the mass of the nuclei is much larger than the mass of the electron, the electronic motion is faster, and the nucleus experiences a smeared out effective potential from the motion of the electrons. When Eq. 2.4 is plugged into the the time-dependent Schrodinger equation, multiplied with $\Psi_e^{i*}(r, R)$ and integrated over all electronic coordinates, one obtains a coupled differential equation. Neglecting the coupling between different nuclear states (represented by the off-diagonal terms of the non-adiabatic coupling operator) gives rise to the adiabatic approximation. Finally, setting the diagonal elements of the coupling operator to zero leads to complete decoupling of the nuclear motion from the electronic motion, therefore giving rise to the Born-Oppenheimer approximation.[25]

The complete decoupling of the nuclear and electronic motion then allows one to write the complete wavefunction as $\Psi(r, R) = \Psi_e(r; R)\Psi_N(R)$

The total energy Hamiltonian is given as

$$\hat{H_N} = -\sum_{i=1}^{N} \frac{\hbar^2}{2M_i}\nabla_i^2 + H_e(R) \tag{2.5}$$

where,

The nuclear wavefunction can be obtained by solving the nuclear Schrodinger equation as

$$\hat{H}_N \left|\Psi_N\right\rangle = -\sum_{i=1}^{N} \frac{\hbar^2}{2M_i}\nabla_i^2 \left|\Psi_N\right\rangle + E_e(R) \left|\Psi_N\right\rangle = E \left|\Psi_N\right\rangle \tag{2.6}$$

where $E = T_N + E_e(R)$

The electronic energy $E_e(R)$ depends parametrically on the nuclear coordinates R. Hence it determines an effective potential energy surface (PES) for various nuclear configurations denoted by R. One of the main motives of solving the Schrodinger equation is to sample the PES, which in turn contains important information about the reactivity of a system.

However, the Schrodinger equation is not exactly solvable for systems containing more than two particles. In fact, the only physically relevant systems for which the time independent Schrodinger equation can be exactly solved is the isolated H atom, and the isolated $H_2{}^{2+}$ systems. For N particle systems, having 3N degrees of freedom, the Schrodinger equation is not solvable analytically, and numerical solutions are computationally intractable. Hence there is a need for alternative, computationally less expensive methods to solve the time-independent Schrodinger equation. One such method is Density Functional Theory (DFT).

2.2 Density Functional Theory

The basis of Density Functional Theory is in the two Hohenberg-Kohn theorems.[26] The first theorem states that the external potential, V_{ext} (hence all associated properties of a system) is uniquely determined (upto an additive constant) by the ground state electron density, $n_0(r)$. The second Hohenberg-Kohn theorem states that a total energy functional $E[n(r)]$ can be defined for any V_{ext} in terms of the electron density $n(r)$, and the value of the functional

at the global minimum of $n(r)$ denoted by $n_0(r)$ gives us the ground state energy for the system, E_0. The Hohenberg-Kohn theorems however do not lead to the expression for the the total energy functional $E[n(r)]$. The energy functional is obtained and solved using the Kohn-Sham ansatz.

In the Kohn-Sham (KS) approach the many-body electron-nuclei system of N particles is reduced into a simpler system of N non-interacting particles moving in an effective potential.[27] The kinetic energy (T) for the non-interacting N-electron system can be written as

$$T = -\frac{1}{2}\sum_{N}\sum_{k}\langle\psi_i^k|\,\nabla^2\,|\psi_i^k\rangle = -\frac{1}{2}\sum_{N}\sum_{k}|\nabla\psi_i^k|^2 \tag{2.7}$$

where ψ_i^k is the wavefunction for the i-th electron in the k-th orbital. The electron density $n(r)$ is defined as $n(r) = \sum_N \sum_k |\psi_i^k(r)|^2$. The Coulomb interaction is represented through the Hartree functional ($E_H[n]$) and has the following form

$$E_H[n] = \frac{1}{2}\int d^3r d^3r' \frac{n(r)n(r')}{|r-r'|} \tag{2.8}$$

Since an effective potential is assumed, the electron-electron repulsion which is effectively a many-body interaction is represented by an exchange-correlation functional of the density, $E_{xc}[n]$, which can further be represented in terms of an exchange correlation energy density $\epsilon_{xc}[n]$ as

$$E_{xc}[n] = \int dr n(r)\epsilon_{xc}([n], r) \tag{2.9}$$

The KS energy functional can be written as

$$E[n] = T[n] + \int dr V_{ext}(r)n(r) + E_H[n] + E_{RR} + E_{xc}[n] \tag{2.10}$$

where E_{RR} is the nucleus-nucleus interaction term.

The exchange-correlation functional is not analytically defined since it is only an approximation to the many-body interactions. It can be modelled in various ways, one of the most commonly used ones being the Generalized Gradient Approximation (GGA).[28] In GGA the exchange-correlation energy density, ϵ_{xc}, is represented as a function of the density at a point

$(n(r))$, as well as the gradient of the density at that point (∇n). Therefore E_{xc}^{GGA} can be written as

$$E_{xc}^{GGA} = \int d^3 r n(r) \epsilon_{xc}(n, |\nabla n|) \tag{2.11}$$

Using the variational principle and the Kohn-Sham energy functional the Kohn-Sham equations can be obtained as, $(H_{KS}^k - \epsilon_{KS}^k)\psi_{KS}^k(r) = 0$, where $\psi_{KS}^k(r)$ are the KS orbitals, ϵ_{KS}^k are the KS eigenvalues, and H_{KS}^k is the KS Hamiltonian defined as

$$H_{KS}^k(r) = -\frac{1}{2}\nabla^2 + V_{ext}(r) + \frac{\delta E_H}{\delta n(r,k)} + \frac{\delta E_{xc}}{\delta n(r,k)} \tag{2.12}$$

$$V_{KS} = V_{ext}(r) + \frac{\delta E_H}{\delta n(r,k)} + \frac{\delta E_{xc}}{\delta n(r,k)} \tag{2.13}$$

The Kohn-Sham potential, V_{KS}, depends upon the exchange-correlation potential and the Coulomb potential, both of which depend upon the electron density. The electron density in turn depends on the KS wavefunction which is the eigenvector of the KS Hamiltonian. Therefore, the KS equation needs to be solved self-consistently, starting from an initial guess of electron density.

In solids, the periodicity of the system allows one to solve the KS equations for a unit cell and propagate these solutions periodically throughout the lattice.[29] Using Bloch's theorem, the wavefunction at any point in the cell can be written as a product of a periodic function, $\psi(r)$, having the periodicity of the lattice vector R and a plane-wave like part with a momentum vector k as,

$$\psi(R + r) = \exp[ik.R]\psi(r) \tag{2.14}$$

The wavefunction $\psi(r)$ can be expanded using a plane wave basis set with wave vector k in the reciprocal space, using reciprocal lattice vectors G, as

$$\psi(r) = \sum_G c_{k+G} \exp[i(k + G).r] \tag{2.15}$$

where c_{k+G} is the co-efficient of expansion.

The wavefunctions at nearby points in the reciprocal space are assumed to be approximately identical. Hence, the electronic wavefunctions are calculated at a finite set of points

in the reciprocal space, called k-points that lie in the irreducible Brillouin Zone. The problem of calculating the wavefunction as an infinite superposition of plane waves is solved by using a kinetic energy cutoff on the plane wave basis set, since it is observed that basis vectors with very high kinetic energy contribute very less to the overall wavefunction for well-behaved potentials.[29]

The core electrons are tightly bound to the nucleus and therefore they do not influence the electronic properties of materials which are mostly governed by the valence electron wavefunctions. Hence, to understand material properties one can effectively treat the core electrons as frozen electrons which do not participate in chemical processes. This allows one to replace the nuclear charge with an effective nuclear charge due to the shielding of the nucleus from the valence electrons by the core electrons. The wavefunctions for the valence electrons have nodes near the nucleus and therefore they need to be expanded using large plane-wave basis sets near the nucleus. The pseudopotential method circumvents the problem of using large basis sets by replacing the electron-ion potential by a pseudopotential which is weak in the core of the atom, and is unaltered in the valence shell. The pseudopotential approximation smoothens the wavefunction in the core region by replacing it with a pseudo-wavefunction. The pseudo-wavefunction is smooth near the nucleus but is exactly identical to the original wavefunction in the valence region. The pseudopotential approximation therefore allows the use of smaller, finite plane wave basis sets which improves the computational efficiency.[29] According to the norm-conserving criteria of pseudopotentials, the norm of the pesudo-wavefunction should be equal to the norm of the true wavefunction in both the core and the valence regions. In Ultrasoft pseudopotentials however the norm conservation criterion of the wavefunction in the core region is relaxed which allows for convergence using smaller basis sets. There is an associated charge augmentation in the core region and a larger cutoff is required to converge the charge density in case of ultrasoft pseudopotentials.[30]

In the case of metallic systems, at 0 K, electronic occupations change discontinuously across the Fermi level. To be able to model the discontinuity correctly, a dense set of k-points is required. A smearing parameter introduces a fictitious electronic temperature to smoothen out the discontinuous electron occupation at Fermi level. This helps to improve convergence with respect to a chosen k-point sampling.[31]

In this study, density functional theory was used to explore the mechanism of methane activation. The calculations were done using Quantum ESPRESSO software (v6.8)[32,.33] The

electron-ion interactions were modelled using ultrasoft pseudopotentials.[30] The valence shell configurations of the elements are:

Ti: [Ar] $3d^2$ $4s^2$ $4p^0$, C: [He] $2s^2$ $2p^2$, H: $1s^2$

A Perdew-Burke-Ernzerhof (PBE)[34] implementation of the generalized gradient approximation (GGA) exchange-correlation functional was used. A plane wave basis set was used with a kinetic energy cutoff of 55 Ry for the wavefunction, and a charge density cutoff of 480 Ry. A Marzari-Vanderbilt smearing with a smearing width of 0.007 Ry was used to speed up the calculation.[35] For bulk TiC, a $12 \times 12 \times 12$ Monkhorst-Pack grid was used to sample the Brillouin zone.

2.3 Surface Models

The TiC(001) surface has been observed to more stable than the other terminations of the TiC surface such as TiC(111)C/Ti-terminated surfaces,[36] indicating that the TiC(001) surface occurs more frequently under experimental conditions. Therefore, the (001) surface is chosen to study the effect of vacancies on the reactivity of the CH_4 molecule.

The TiC(001) surface has been modelled as a slab consisting of 5 layers of Ti and C atoms, of which the bottom 2 layers are constrained to the bulk interlayer separations. The top layer of the slab is assumed to represent the surface, while the lower layers are made to converge to the bulk interlayer separations, thereby representing bulk TiC as one moves away from the surface. Since periodic boundary conditions in (x, y, z) directions is built into the Quantum ESPRESSO code, the periodicity of the structure needs to be broken in the (001) direction in order to obtain the TiC(001) surface. The unit cell is padded with vacuum of 18 Å in the z-direction order to break the periodicity in the direction perpendicular to the slab surface. The length of the vacuum is optimized to ensure that periodic images of the unit cell in the z-direction do not interact with each other.

To understand the strength of adsorption when molecules adsorb on the surface, the adsorption energies of the molecules are calculated using the formula,

$$E_{ads} = E_{surf+mol} - E_{surf} - E_{mol} \tag{2.16}$$

where $E_{surf+mol}$ is the total energy of the surface with the molecule adsorbed on it, E_{surf} is the total energy of the clean surface, and E_{mol} is the energy of the free molecule.

2.4 Zero Point Energy and Free Energy Corrections

We obtain the ground state electronic energy of a system from DFT calculations. To determine the total ground state energy of the system at 0 K, the zero-point energy of the system should be added to the ground state electronic energy of the system. The zero-point energy is obtained through the formula, $E_{ZPE} = \sum_i \frac{1}{2}\hbar\omega_i$, where, ω_i represents the frequency of the i-th phonon mode of the system. The phonon frequencies are calculated using Density Functional Perturbation Theory[37] (DFPT) as implemented in Quantum ESPRESSO. Phonon calculations are performed at the gamma point. A partial phonon calculation is performed to calculate only the normal modes corresponding to the molecules of the first layer of the surface and the molecule adsorbed on it. It is assumed that the subsurface layers beyond the first layer do not contribute appreciably to the normal modes of the molecule.

The Born-Oppenheimer (BO) approximation allows the separation of the nuclear and electronic degrees of freedom, and the parameterisation of the ground state electronic energy of the system in terms of the nuclear coordinates, $\mathbf{R}$, as E($\mathbf{R}$). The force acting on the system at equilibrium is given by

$$F(\mathbf{R}) = -\frac{\partial E(\mathbf{R})}{\partial \mathbf{R}} = 0 \tag{2.17}$$

The forces on the I-th atom in the system is calculated using the Hellmann-Feynman (HF) theorem as

$$F_I = -\left\langle \Psi(R) \right| \frac{\partial H(R)}{\partial R_I} \left| \Psi(R) \right\rangle \tag{2.18}$$

where R denotes the nuclear coordinates.

In DFPT, the external potential can be modelled using linear response theory as

$$V_\lambda(r) = V_0(r) + \sum_i \lambda_i v_i(r) \tag{2.19}$$

where λ_i is the perturbation on the i-th atom, and v_i is the potential experienced by the i-th atom.

Using the HF theorem we can calculate the forces for every perturbation λ_i as,

$$\frac{\partial E(\lambda)}{\partial \lambda_i} = \int n_\lambda(r) v_i(r) dr \tag{2.20}$$

The interatomic force constants can be calculated as

$$\frac{\partial^2 E(\lambda)}{\partial \lambda_i \partial \lambda_j} = \int \frac{\partial n_\lambda(r)}{\partial \lambda_j} v_i(r) dr \tag{2.21}$$

The frequencies ω are obtained using the following equation

$$det|\frac{1}{\sqrt{M_I M_J}} \frac{\partial^2 E(\lambda)}{\partial^2 \lambda_I \lambda_J} - \omega^2| = 0 \tag{2.22}$$

where M_I and M_J are the masses of the I-th and J-th nuclei.

The ZPE corrected adsorption energy ($E_{ads(corr)}$) is calculated as,

$$E_{ads(corr)} = E_{surf+mol} + E_{ZPE}^{surf+mol} - E_{surf} - E_{ZPE}^{surf} - E_{mol} - E_{ZPE}^{mol} \tag{2.23}$$

Similarly for calculating the ZPE corrections for all other intermediate and transition state configurations we use the following equation,

$$E_{corr} = E_{final} + E_{ZPE}^{final} - E_{initial} - E_{ZPE}^{initial} \tag{2.24}$$

where, E_{final} is the final energy of the system, $E^{initial}$ is the initial energy of the system, and E_{ZPE}^{final}, $E_{ZPE}^{initial}$ are the ZPEs of the final and initial states.

In order to compute the spontaneity of a reaction at finite temperature and pressure, the Gibbs free energies of the important reaction intermediates and the transition states is

calculated. The Gibbs free energy (G) is given by

$$G = H - TS \tag{2.25}$$

where H and S denote the enthalpy and entropy, respectively. T is the temperature.

In order to compute Gibbs free energy from first principles, the ZPE correction, the enthalpic temperature correction and the entropic contributions are required for the system. In order to compute these, the prescription suggested by Bendavid *et al.*[38] has been followed. The vibrational entropy (S_v(T)) for the surface is calculated using the following equation

$$S_v(T) = k_B \left[\sum_k ln \frac{1}{1 - e^{-\theta_{\nu,k}/T}} + \sum_k \frac{\theta_{\nu,k}}{T} \frac{1}{e^{\theta_{\nu,k}/T} - 1} + 1 \right] \tag{2.26}$$

where

$$\theta_{\nu,k} = \frac{h\nu_k}{k_B} \tag{2.27}$$

where ν_k is the frequency of the k-th vibrational mode, obtained from the phonon calculations for the system.
Similarly, the change in vibrational enthalpy ($H_v(T) - H_v(0)$) of the surface as a function of temperature is calculated using the equation,

$$H_v(T) - H_v(0) = k_B T \left[\sum_k \frac{\theta_{\nu,k}}{T} \frac{1}{e^{\theta_{\nu,k}/T} - 1} + 1 \right] \tag{2.28}$$

The free energy correction ΔG at a temperature T (in K) can then be calculated as,

$$\Delta G = E_{ZPE} - TS_v + H_v(T) - H_v(0) \tag{2.29}$$

The free energy of reaction $E_{rxn(corr)}$ for each step is,

$$E_{rxn(corr)} = E_P + \Delta G_P - E_R - \Delta G_R \tag{2.30}$$

where E_P (E_R) is the DFT energy of the product (reactant) and ΔG_P (ΔG_P) is the free

energy correction for the product (reactant) configuration.

Similarly the free energy of activation $E_{A(corr)}$ can be calculated as,

$$E_{A(corr)} = E_{TS} + \Delta G_{TS} - E_I - \Delta G_I \tag{2.31}$$

where E_{TS} (E_I) is the DFT energy of the transition state (intermediate) and ΔG_{TS} (ΔG_I) is the free energy correction for the transition state (intermediate) configuration.

In order to calculate the free energy of adsorption $E_{ads(corr)}$ of the molecules on the catalyst surface we use the following formula,

$$E_{ads(corr)} = E_{surf+mol} + \Delta G_{surf+mol} - E_{surf} - \Delta G_{surf} - E_{mol} - \Delta G_{mol} \tag{2.32}$$

where $E_{surf+mol}$ is the total energy of the surface with the molecule adsorbed on it, E_{surf} is the energy of the free catalyst surface and E_{mol} is the energy of the molecule in the gaseous phase. $\Delta G_{surf+mol}, \Delta G_{surf}$ and ΔG_{mol} are the free energy corrections for the surface with molecule, free surface, and gas phase molecule respectively.

Since CH_4 is a non-linear molecule, the calculation of the rotational entropy of CH_4 is non-trivial. The standard entropy and enthalpy of the CH_4 and the C_2H_2 molecules in the gas phase is obtained from standard experimental data, which is claimed to match closely to theoretical calculations.[39]

Free energy corrected activation barriers and reaction energies are calculated for every reaction step at a range of temperatures between 0 K to 1200 K.

2.5 Charge Analysis

Charge Analysis calculations are done using the Density Derived Electrostatic and Chemical (DDEC) method developed by Manz and co-workers.[40] Net atomic charges were calculated using the DDEC6 method implemented in the Chargemol programme.[40] Net atomic charges (NAC) are defined as the difference between total number of protons and total number of electrons in an atom. Hence a negative NAC denotes an excess electron density on the atom, whereas a positive NAC denotes reduced electron density on an atom. DDEC belongs to the

family of methods called Atom in Molecule (AIM) methods which are used to assign charges to atoms in molecular systems. DDEC uses a vectorized charge partitioning method in order to approximately calculate the electrostatic potential surrounding an atom in a molecule. In vectorized charge partitioning the probability of an electron belonging to an atom A is represented as a vector $w_A(r_A)$ containing the weights or the probability of obtaining the electron at a distance r_A from the nucleus.

$$\frac{\rho_A(\vec{r}_A)}{\rho(\vec{r})} = \frac{w_A(r_A)}{W(\vec{r})} \tag{2.33}$$

where, W()=$\sum_{A,L} w_A(r_A)$, and L is the reciprocal lattice vector.

This reduces the dimensionality of the charge partitioning method. Instead of calculating the relative electron density, $\rho_A(\vec{r}_A)/\rho(\vec{r})$, which is a three dimensional vector, one needs to only calculate the weights (which is a one-dimensional value) as a function of the distance.[40]

The charge transfer between the surface and the adsorbed molecule is calculated according to the following equation,

$$Q_{CT}(R) = Q_{surf+mol}(R) - Q_{surf}(R) - Q_{mol}(R) \tag{2.34}$$

where $Q_{\mathrm{CT}}(R)$ is the charge transfer for a particular arrangement of atoms R, evaluated as the difference in the electron density of the surface with the molecule adsorbed on it ($Q_{\mathrm{surf+mol}}(R)$), the electron density on the surface with the surface atoms in the same geometry as when the molecule is adsorbed on the surface($Q_{\mathrm{surf}}(R)$) and the electron density on the molecule in the same configuration in which it adsorbs on the surface($Q_{mol}(R)$).

2.6 Transition State Theory and Nudged Elastic Band calculations

Transition state theory allows one to calculate the rate of chemical reactions. The central assumption of Transition State Theory is that the system follows the Born-Oppenheimer Approximation and hence the Potential Energy Surface (PES) can be defined as a function of nuclear coordinates. Transition State Theory (TST) is based on the following assumptions,

a) the reactant is in an equilibrium Boltzmann distribution in its potential well, b) the transition state is a surface of infinitesimal thickness that separates the initial and final states and has a dimensionality that is 1 less than the dimensions of the PES, c) there is negligible quantum tunnelling.[41]

Harmonic TST (HTST) assumes that the PES is smooth enough such that the potential at a stationary point can be locally approximated as a harmonic potential. This allows one to calculate the partition functions analytically.[41] The HTST rate constant is defined as

$$k_{HTST} = \frac{k_B T}{h} \frac{\prod_i{}^{\text{D-1}}(1 - e^{-\frac{h\nu_{i,TS}}{k_B T}})}{\prod_j{}^{\text{D}}(1 - e^{-\frac{h\nu_{j,SP}}{k_B T}})} . e^{-\frac{\Delta E_a}{k_B T}} \tag{2.35}$$

where i and j are the degrees of freedom in the TS and the initial state (denoted by SP) respectively, and D denotes the total number of degrees of freedom of the initial configuration.

Assuming $h\nu_i, h\nu_j << k_B T$ for all i and j,

$$k_{HTST} = \frac{\prod_i{}^{\text{D-1}}\nu_i{}^{\text{TS}}}{\prod_j{}^{\text{D}}\nu_j{}^{\text{SP}}} . e^{-\frac{\Delta E_a}{k_B T}} \tag{2.36}$$

To be able to calculate the rate constant according to HTST one needs to obtain the total energy and the vibrational modes of the first order saddle point on the PES. The activation energy ΔE_a is the difference in energies between the saddle point and the initial state. The Nudged Elastic Band method[42] (NEB) is used to obtain the first order saddle point when both the initial state (IS) and the final state (FS) configurations are known. The NEB method involves defining a minimum energy path (MEP) from the initial state to the final state. The saddle point is the highest energy configuration along the MEP.

In the NEB method a number of images of the system representing the chemical reaction taking place are created and are connected by springs. This represents the initial guess for the path leading from the IS to the FS. The force on each image is equal to the sum of the perpendicular component of the true force and the parallel component of the spring force. The component of the force along the MEP is iteratively minimized to zero for each image. The NEB calculation proceeds through a series of force minimization steps on every image in the MEP in order to satisfy this constraint.

The total force on the i-th image is given as,

$$F_i = -\nabla E(R_i)|_\perp + F_i^{\mathrm{s}}.\hat{\tau}_i\hat{\tau}_i \tag{2.37}$$

where $E(R_{\mathrm{i}})$ is the energy of the i-th image, and F_i^{s} is the spring force acting on the i-th image, τ_{i} is the tangent to the path at the i-th image. The perpendicular component of the force is obtained as

$$\nabla E(R_i)|_\perp = \nabla E(R_i) - \nabla E(R_i).\hat{\tau_{i\|}}\hat{\tau_{i\|}} \tag{2.38}$$

The parallel component of the spring force for an image is calculated as

$$F_i^{\mathrm{s}} = k(|R_{i+1} - R_i| - |R_i - R_{i-1}|).\hat{\tau}_i \tag{2.39}$$

$\hat{\tau}_i$ is calculated according to the following equation

$$\tau_i = \frac{R_i - R_{i-1}}{|R_i - R_{i-1}|} + \frac{R_{i+1} - R_i}{|R_{i+1} - R_i|} \tag{2.40}$$

Although the NEB method provides an estimate of the MEP, it does not always provide the geometry of the first order saddle point along the MEP. In order to obtain the highest energy first order saddle point, which represents the transition state, the Climbing Image-NEB method is used. In the Climbing-Image Nudged Elastic Band Method (CI-NEB)[43] the image having the highest energy along the MEP is allowed to move uphill in energy. The spring force on this image is set to zero, so that the only force acting on this image is the negative of the parallel component of the true force. This allows the image to reach its maximum energy along the MEP and provides a more accurate estimate of the saddle point configuration and the activation energy. The equation for the force acting on the highest image is given as,

$$F_{imax} = -\nabla E(R_{imax}) + 2\nabla E(R_{imax}).\hat{\tau_{imax}}\hat{\tau_{imax}} \tag{2.41}$$

where the *imax* index refers to the image number having the highest energy along the MEP.

NEB and CI-NEB calculations were done using Quantum ESPRESSO for every reaction step considered in this study. A force convergence criteria of 0.05 eV/Å was used, with 5-7 images depending on the MEP length. The Broyden-Fletcher-Goldfarb-Shanno (BFGS)

and conjugate gradient minimization schemes were used to reach the MEP from an initial interpolated guess path.

Chapter 3

Results and Discussion

3.1 CH_4 molecule

The CH_4 molecule was optimized in the gas phase. A bond length of 1.09 Å was obtained. This compares well against the experimentally measured equilibrium bond length of 1.08 Å and the theoretically calculated value of 1.09 Å obtained using a PBE functional.[44] The calculated phonon modes have frequencies of 3068.03 cm^{-1}, 2939.69 cm^{-1}, 1498.12 cm^{-1} and 1279.81 cm^{-1}. These values are within a 100 cm^{-1} range of the experimentally reported values of 3156.8 cm^{-1}, 3025.5 cm^{-1}, 1582.7 cm^{-1} and 1367.4 cm^{-1}.[45] A HOMO-LUMO gap of 8.91 eV is obtained. This is much lower than the experimental band gap of 20 eV,[46] consistent with the fact that the PBE functional underestimates band gaps.

3.2 Bulk TiC

Bulk TiC has a fcc structure (Fig. 3.1(a)). The calculated lattice parameter of 4.34 Å compares well against the experimentally reported value of 4.33 Å and that reported in other DFT calculations.[36] A Ti-C bond length of 2.16 Å is observed which matches with the experimental value of 2.16 Å.[36] The band structure and density of states were plotted with respect to the Fermi energy of the system (Fig. 3.1(b)). The results of the projected density of states calculations depict the contributions from Ti-3d orbitals and C-2p orbitals. The

valence band has significant contributions from the Ti(3d) and C(2p) orbitals, while the conduction band has major contributions from the Ti(3d) orbitals and only minor contributions from C(2p) states. The Fermi energy has a non-zero DOS which indicates that the material is predominantly metallic in nature.

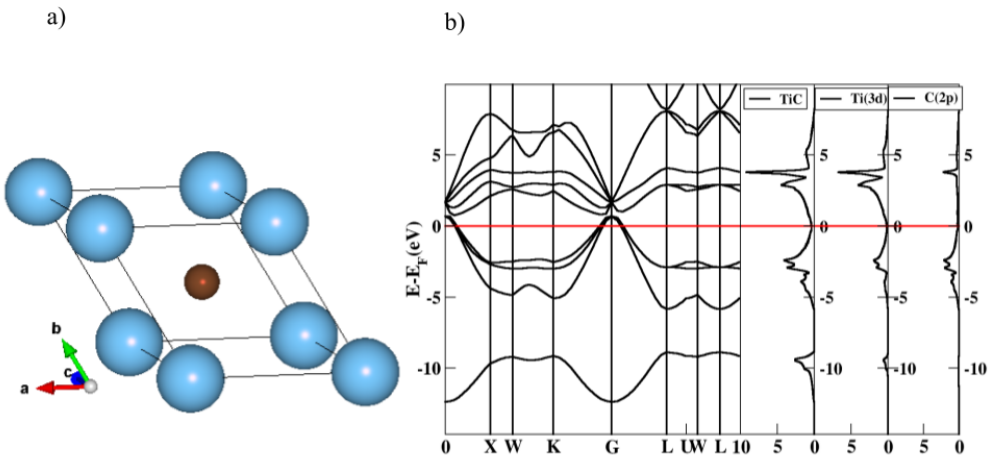

Figure 3.1: (a) TiC bulk primitive unit cell and (b) TiC bulk band structure and total density of states (second column). The third and fourth columns show contributions from Ti(3d) and C(2p) orbitals.

3.3 TiC(001) surfaces

Amongst the different TiC surfaces, previous studies have shown that the (001) surface (Fig. 3.2(a)) to be the most stable one.[36] In order to study C vacancies on TiC(001) surface we consider a $2\sqrt{2} \times 2\sqrt{2}$ surface supercell. In order to study the effect of concentration of carbon vacancies on methane activation, we have considered two cases - a single C vacancy, Fig. 3.2(b) (12.5% C-vacancy concentration), and, two C vacancies (divacancy) located adjacent to each other, Fig. 3.2(c) (25% C-vacancy concentration). We have chosen these based on previous literature reports.[36]

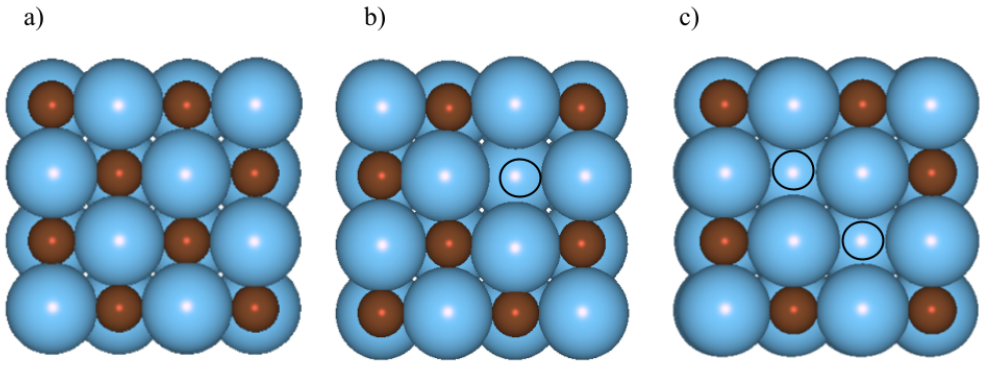

Figure 3.2: (a) Pristine TiC(001) surface, (b) TiC(001) surface containing a single C-vacancy, (c) TiC(001) surface containing a C divacancy. The black open circles denote the position of the C-vacancy.

3.4 CH_4 activation on single C vacancy

All the energies reported in the following section concerning CH_4 adsorbtion and dissociation on the single vacancy are ZPE corrected and reported at 0 K, unless otherwise mentioned.

3.4.1 Adsorption of CH_4

The initial step in the activation of the methane molecule involves its physisorption on the surface. Amongst the different configurations considered in this study, the S0 configuration (Fig. 3.3), with one -CH bond pointing towards the defect, while the rest three oriented away from the surface, was found to the be the lowest energy conformation for adsorption of CH_4 on the surface with single C-vacancy. Methane binds to this surface with an adsorption energy of -0.26 eV. The H atom facing the surface has a H-surface distance of 1.36 Å. Compared to gas phase methane, this -CH bond of the physisorbed methane molecule is elongated to 1.12 Å. The other three C-H bonds that are oriented away from the surface have an average bond length of 1.09 Å, which is similar to the C-H bond length in gaseous CH_4. The elongation of the C-H bond and the CH_4 orientation are similar to those observed in methane's physisorption over carbon vacancies in non-stoichiometric Ti_2C.[9]

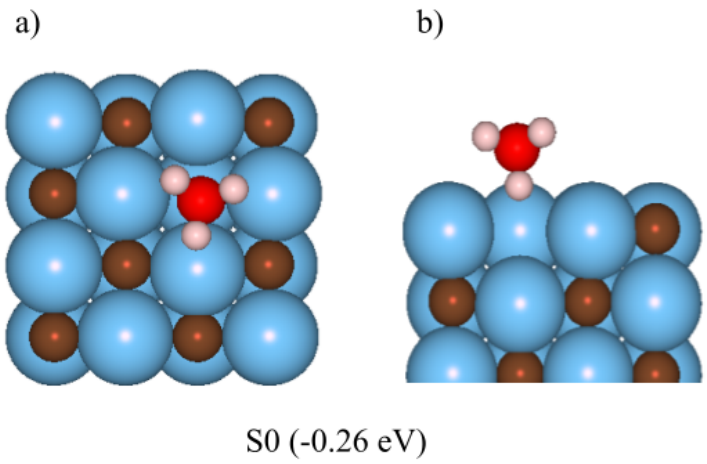

Figure 3.3: a) Top view and b) side view for CH_4 adsorption on a TiC(001) surface with a single vacancy. The pink atoms represent H atoms and the red spheres represent the C atom belonging to the substrate CH_4 molecule.

3.4.2 Activation of physisorbed CH_4

Following the adsorption of CH_4 on the surface the activation of the C-H bonds is studied sequentially until CH_4 is fully dissociated to form C + 4H. This allows us to understand the stability of various $CH_x (x = 1 - 4)$ species on the surface, which in turn allows us to predict whether the catalyst could be used for direct conversion of methane to a valuable product or not.

3.4.3 $CH_4^\star \rightarrow CH_3^\star + H^\star$

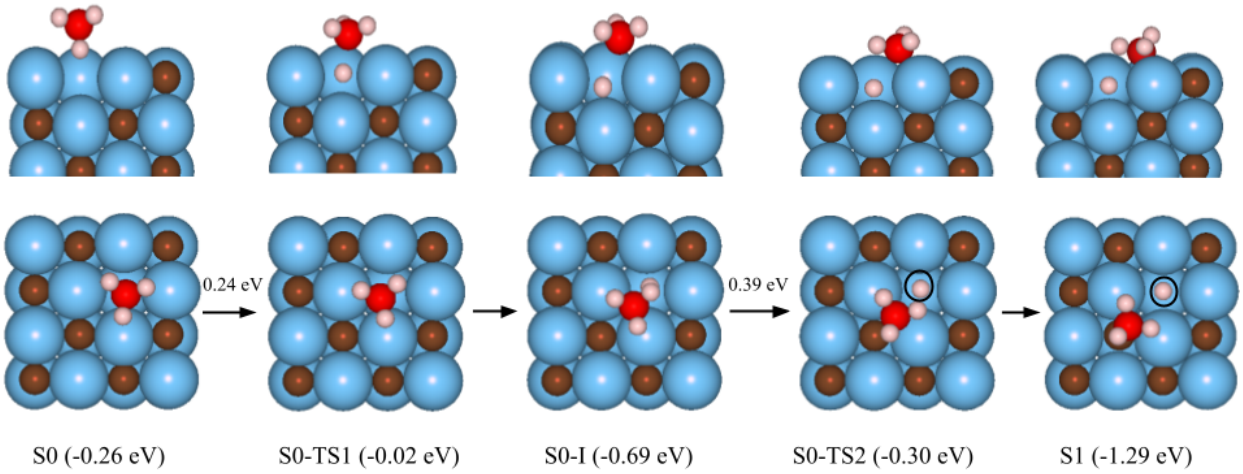

Figure 3.4: Side and top views of the reaction profile for $CH_4^\star$ (S0)$\rightarrow$ $CH_3^\star$+$H^\star$(S1) on single vacancy. The energies in parenthesis represent the ZPE corrected energy of the state with respect to the gas phase energy of the CH_4 molecule and the energy of the clean surface.

The physisorbed molecule in the S0 configuration, with a ZPE corrected adsorption energy of -0.26 eV is chosen to study the first C-H bond activation. In the final state (S1), the dissociated H atom occupies the carbon vacancy and the methyl radical binds to one of the C atoms surrounding the defect (Fig. 3.4). The two C-H bonds of the methyl radical, closer to the vacancy are further elongated elongated (1.14 Å) compared to the physisorbed S0 configuration of methane. In contrast, the C-H bond facing away from the vacancy has a bond length of 1.09 Å, similar to the molecule in the gas phase. The C atom of the CH_3 group is located at a vertical distance of 1.38 Å from the surface. The dissociated H atom occupying the carbon vacancy is located at a distance of 2.13 Å from the Ti atom in the second layer.

This bond dissociation step corresponds to a ZPE corrected reaction energy of -1.03 eV. This is more exothermic than the first C-H bond dissociation energy on clean TiC(001) of -0.25 eV (without ZPE correction),[8] but less exothermic than the first C-H bond dissociation energy in Ti_2C (-1.18 eV).[9] This step proceeds through the formation of an intermediate (S0-I) where the CH_3 group occupies the bridge site in between two Ti atoms surrounding the defect. The transition state (S0-TS1) leading up to the intermediate corresponds to the breaking of the C-H bond, and is associated with an activation energy of 0.24 eV. The

second transition state (S0-TS2) leading from the intermediate S0-I to the final CH_3^* + H^* (S1) configuration corresponds to an activation energy of 0.39 eV and is associated with the rotation of the CH_3 group.

3.4.4 $CH_3^\star + H^\star \rightarrow CH_2^\star + 2H^\star$

Following the cleavage of the the first C-H bond the next step is assumed to be the splitting of a C-H bond in CH_3 to form CH_2 and H. The step (Fig. 3.5) proceeds through an intermediate (S1-I) in which the longest C-H bond with a bond length of 1.14 Å in the CH_3 group breaks and the methylene radical occupies the bridge site in between two Ti atoms around the defect. The transition state (S1-TS1) leading to the intermediate (S1-I), with an activation energy of 0.73 eV, is the rate determining step for the formation of the CH_2 group and corresponds to the breaking of the C-H bond. The activation energy leading up to the second transition state (S1-TS2) is 0.03 eV and involves a the translation of the H atom from the Ti-Ti bridge site in the intermediate S1-I towards the C atom on the surface. In the final configuration (S2), the H atom is adsorbed on top of the C atom adjacent to the vacancy, and the CH_2 moiety is bound to the surface in between a C and a Ti atom surrounding the defect. The surface C-H bond formed in this step has a bond length of 1.13 Å. The CH_2 group is located at a vertical distance of 1.24 Å from the surface. The H atom from the first C-H bond dissociation that was adsorbed on the C-vacancy now moves slightly more towards the Ti atom in the second layer resulting in vertical distance of 2.04 Å from the Ti atom in the second layer. The possibility of the recombination of the two H atoms from the cleavage of the two C-H bonds to form H_2 is also explored. However the final states corresponding to H_2 molecule formation at this stage is highly endothermic (by about 1.46 eV) in comparison to the formation of $CH_2^\star + 2H^\star$ and hence H_2 evolution is not expected to be observed during the course of CH_4 dissociation on the single vacancy.

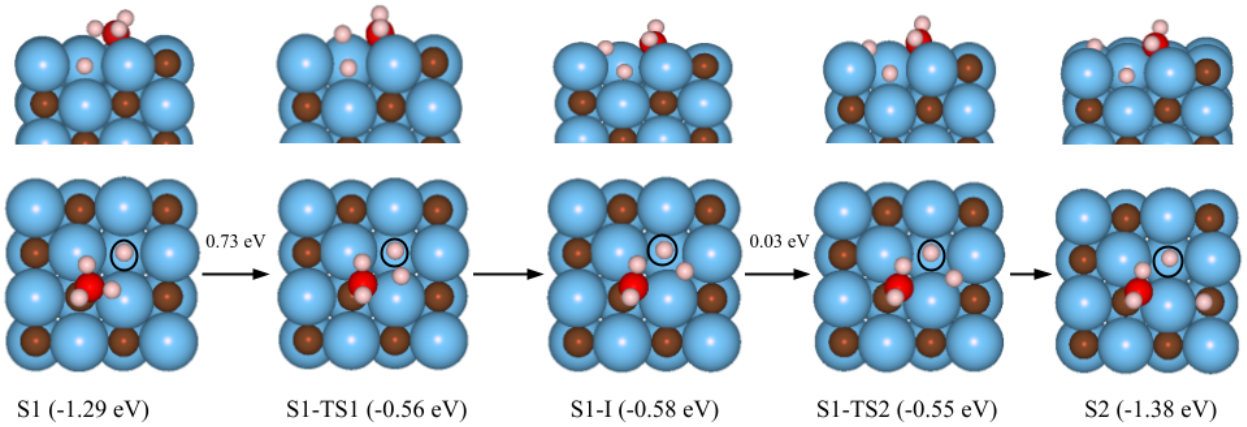

Figure 3.5: Side and top views of the reaction profile for $CH_3^\star$+$H^\star$ (S1) $\rightarrow$ $CH_2^\star$+2$H^\star$ (S2) on single vacancy. The energies in parenthesis represent the ZPE corrected energy of the state with respect to the gas phase energy of the CH_4 molecule and the energy of the clean slab.

3.4.5 $CH_2^\star$+2$H^\star$ $\rightarrow$ $CH^\star$+3$H^\star$

The third C-H bond breaking is endothermic and has a reaction energy of 0.13 eV. The longer C-H bond in $CH_2^\star$ breaks and the dissociated H atom adsorbs on top of one of the C atoms neighbouring the defect to form a CH group (S3) (Fig. 3.6). The CH group binds with one C atom and two Ti atoms on the surface. The C-H bond length for the H atom adsorbed on the surface is 1.18 Å. The C-H bond in the CH moiety is slightly shortened with a bond length of 1.09 Å. This step proceeds through a single transition state (S2-TS) with an activation energy of 0.89 eV corresponding to the breaking of the C-H bond.

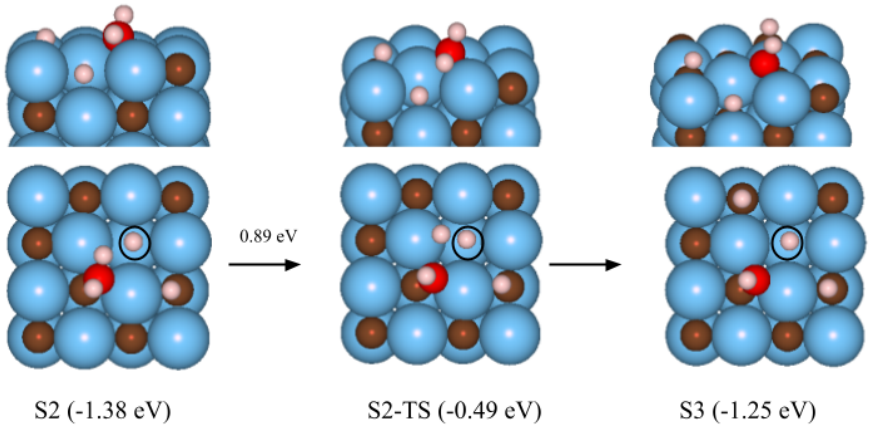

Figure 3.6: Side and top views of the reaction profile for $CH_2^{\star}$+2H* (S2) $\rightarrow$ CH*+3H* (S3) on single vacancy. The energies in parenthesis represent the ZPE corrected energy of the state with respect to the gas phase energy of the CH_4 molecule and the energy of the clean slab.

3.4.6 CH*+3H* $\rightarrow$ C*+4H*

The C atom formed from the final dissociation of the CH group is bonded to two Ti and one C atom on the surface (S4 as depicted in Fig. 3.7 The H atom formed from breaking of the final C-H bond is adsorbed on top of one of the C atoms on the surface, with a C-H bond length of 1.13 Å. In this step all the 3 H atoms adsorbed on top of C-atoms on the surface have identical bond lengths of 1.13 Å. This step is endothermic with a reaction energy of 0.73 eV. The transition state (S3-TS) exhibits an activation energy of 1.69 eV, and corresponds to the breaking of the C-H bond. The reaction profile is depicted in Fig. 3.7

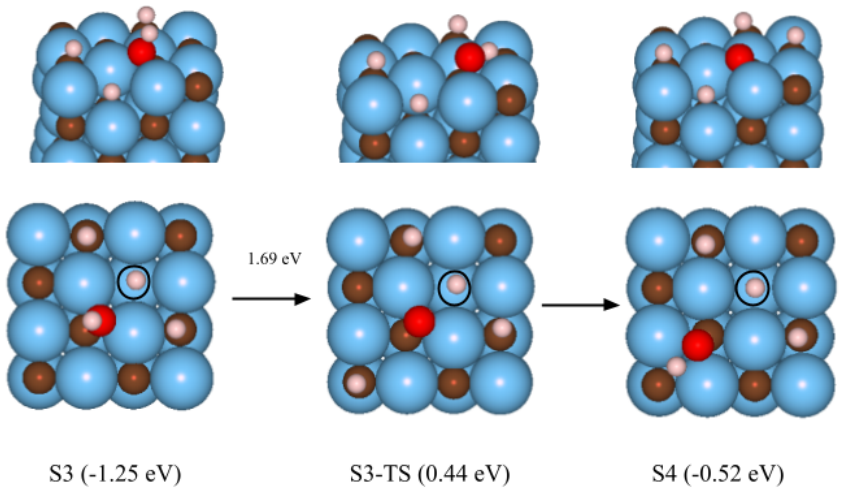

Figure 3.7: Side and top views of the reaction profile for CH*+3H* (S3) → C*+4H* (S4) on single vacancy. The energies in parenthesis represent the energy of the state with respect to the gas phase energy of the CH_4 molecule and the energy of the clean slab.

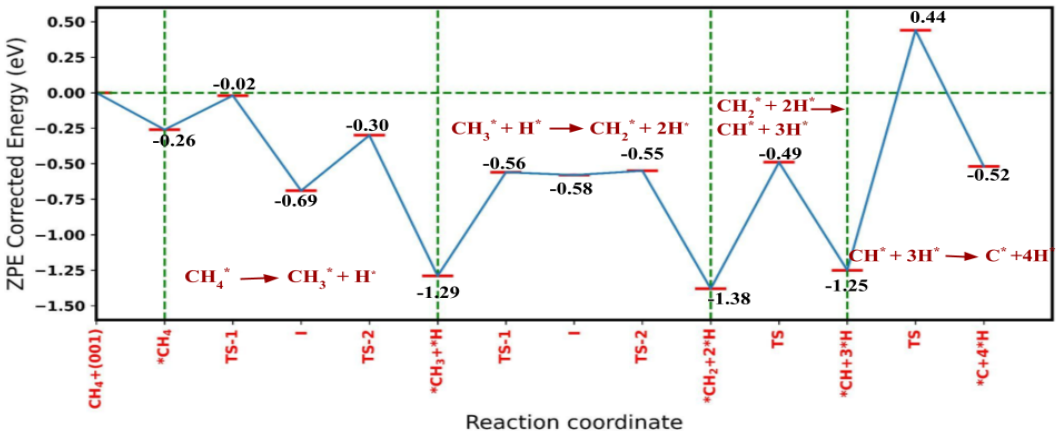

Figure 3.8: Complete Reaction Profile for CH_4* → C*+4H*. The energies represent the ZPE corrected energy of the state with respect to the gas phase energy of the CH_4 molecule and the energy of the clean slab.

3.4.7 Charge Analysis

In order to understand the interaction between the molecule and the surface, we have computed the total density of states (DOS) of the clean surface and the one with methane

adsorbed on it (Fig. 3.9(a)). In addition to the highest occupied molecular orbitals (HOMO) of CH_4 below -6.0 eV, we observe a new state at 0.70 eV above Fermi energy. This state has contributions from the 3d orbitals of the Ti atoms surrounding the C-vacancy and the -CH bond of the adsorbed CH_4 methane molecule as is evident from the plots of the DOS projected on the atomic orbitals (Fig. 3.9(b) and (c)). The integrated local DOS plots plotted in the energy window of (0.45 eV, 0.95 eV) Fig. 3.9(d) shows that the wavefunction corresponding to this state not only has weights on the Ti and C atoms of the surface, but also has a significant weight on the -CH bond of the methane molecule that is interacting with the surface.

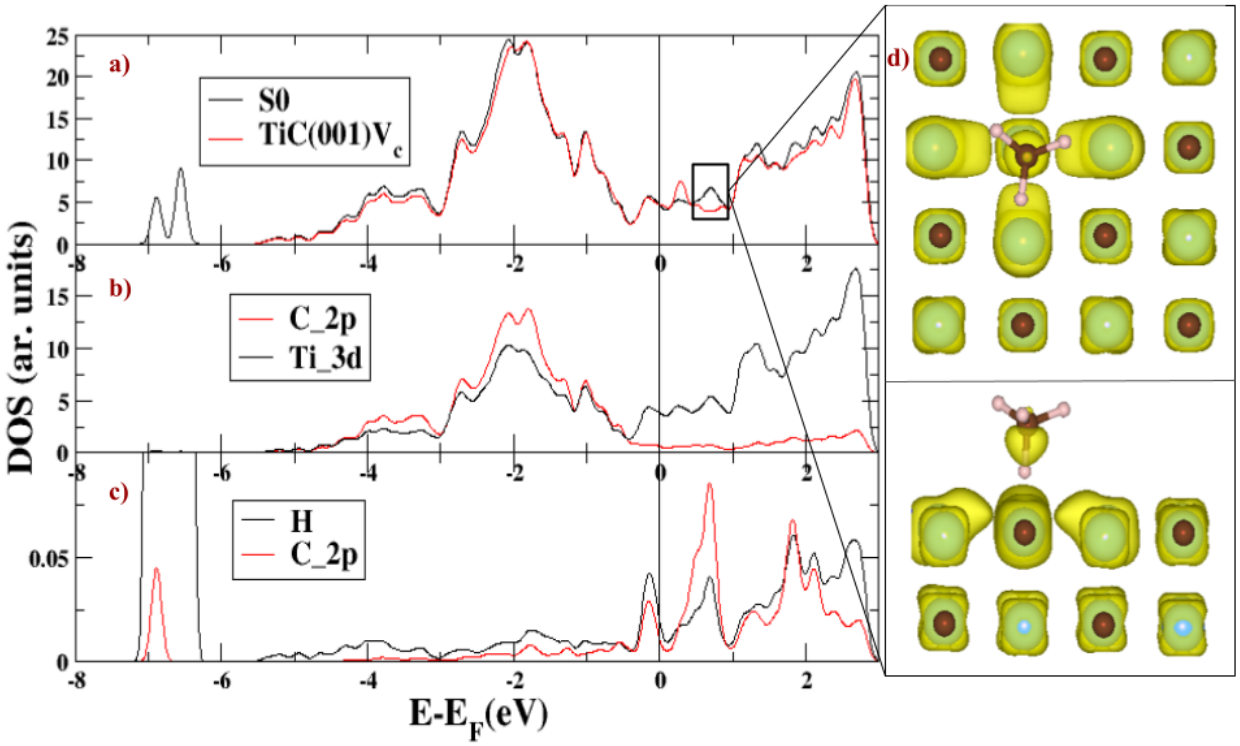

Figure 3.9: Projected Density of States for CH_4 adsorbed on the single vacancy, (a) shows DOS of molecule adsorbed on surface and free surface, (b) shows contributions of Ti(3d), C(2p) and C(2s) orbitals. (c) shows contributions of C(2p), C(2s) and H(1s) of the adsorbed CH_4 molecule. (d) Top view (top panel) and side view (bottom panel) of the ILDOS plot for CH_4 adsorption on a single vacancy in the energy window of (0.45 eV,0.95 eV), visualized at an isovalue of 0.0035.

To understand the mechanism of activation of the CH_4 molecule when it is adsorbed on the surface, a charge density analysis for the S0 configuration is performed.

The charge transfer from the surface to the CH_4 molecule is visualized in Fig. 3.10. The blue lobes represent regions of reduced charge density, and the yellow lobes represent regions of increased charge density. Increased electron density is observed at the C atom of the CH_4 molecule. The blue lobes at the vacancy indicate reduced charge density on the surface compared to the surface with vacancy. This implies that there is some surface charge depletion when the molecule adsorbs on the surface. This indicates that electron density is transferred from the dangling bonds at the defect site to the lowest unoccupied molecular orbitals (LUMO) of the CH_4 molecule.

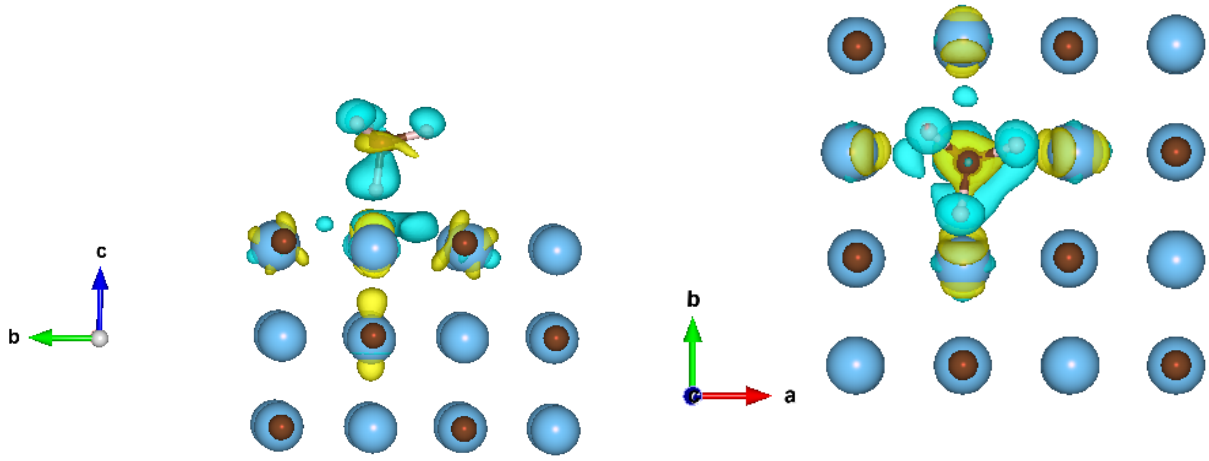

(a) Side View (b) Top View

Figure 3.10: Charge transfer isosurface for CH_4 adsorption on single vacancy, visualized at an isovalue of 0.0021 . Yellow lobes represent increased charge density. Blue lobes represent reduced charge density.

To quantify the amount of charge transferred from the surface to the molecule, the DDEC6 net atomic charges (NAC) for the systems are calculated and the NACs on all the atoms of the CH_4 molecule before and after C-H bond dissociations are compared. When the molecule is adsorbed onto the surface in the S0 configuration, the net charge on the CH_4 group is only slightly negative (-0.07 e), indicating there is negligible electron transfer occurring from the surface to the molecule in the physisorbed configuration. Once the first C-H bond is dissociated the electron density on the H atom that slips into the defect also increases, and remains constant (-0.56 e) thereafter. Initially the C of the CH_4 molecule in the S0 configuration has a charge of -0.58 e, on account of being attached to the 4 less electronegative H atoms, and due to the charge transfer to the molecule from the surface.

When the CH_4 group dissociates to form CH_3 which is covalently bonded to one of the surface C atoms, the negative charge on the C(CH_3) reduces to -0.25 e. The C in CH_2 which is attached to one surface C and a surface Ti has a NAC of -0.52 e. Since the C is now bonded to a less electronegative Ti atom, and draws electron density from the surface Ti, it has a greater electron density. The C atom in CH has a charge of -0.68 e since it is bonded to surface Ti atoms. In the final step, as CH dissociates to form C on the surface, the charge on the C atom goes down to -0.65 e since the C atom only has a coordination number of 3 in this case. The charge on the C atom of the CH_x group in each of the steps in tabulated in Table. 3.1.

Table 3.1: Net Atomic Charges on the C of the $CH_x^\star$(x=0-4)

$CH_4^\star$(C)	$CH_3^\star$(C)	$CH_2^\star$(C)	$CH^\star$(C)	$C^\star$(C)
-0.58	-0.25	-0.52	-0.68	-0.65

3.5 CH_4 activation on divacancies

To compare how the activation and the reactivity of the CH_4 molecule varies depending on the vacancy concentration, we studied CH_4 activation on the divacancy containing surface. All the energies reported are zero-point corrected energy values.

3.5.1 Adsorption of CH_4

On the di-vacancy surface the C:Ti ratio on the surface is 0.75. The two vacancies are formed due to the removal of two carbon atoms that are adjacent to each other. Among all possible combinations of two vacancies on the surface this configuration has been observed to be the most stable divacancy arrangement.[36] On the surface containing divacancies, in the most stable configuration, the CH_4 molecule adsorbs on the Ti-Ti bridge site in between the two vacancies, with one of the H atoms pointing towards the vacancy (Fig. 3.11). Similar to that observed in the single vacancy, the C-H bond pointing into the vacancy is elongated with a bond length of 1.12 Å while those facing away from the surface are unperturbed. The H atom facing the vacancy is at a vertical distance of 1.65 Å from the surface. This configuration corresponds to an adsorption energy of -0.30 eV. The adsorption of CH_4 on this

surface is stronger than that on the single vacancy surface and that on the Ti_2C surface.[9]

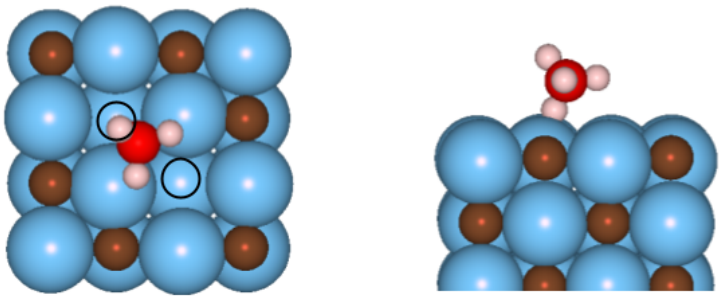

Figure 3.11: Adsorption of CH_4 on surface with divacancy (D0)

3.5.2 Activation of physisorbed CH_4

3.5.3 $CH_4^\star \rightarrow CH_3^\star + H^\star$

The activation of the CH_4 on the surface occurs through the dissociation of the C-H bond pointing towards the surface. The side and top views of the reaction profile is depicted in Fig. 3.12. This step has an activation energy of 0.18 eV. In the transition state (D0-TS) the CH_3 group occupies the Ti-Ti bridge site. In the final configuration (D1), the CH_3 group formed due to activation occupies the top of one of the vacancies, while the H atom occupies the other vacancy. There is a slight barrierless rotation of the CH_3 group as it occupies the vacancy top. The H-subsurface Ti distance for the H atom occupying the vacancy is 2.14 Å. The CH_3 group is located at a distance of 1.40 Å above the surface. This step corresponds to a reaction energy of -1.36 eV. The C-H bonds on the CH_3 group are slightly elongated to 1.11 Å and 1.13 Å.

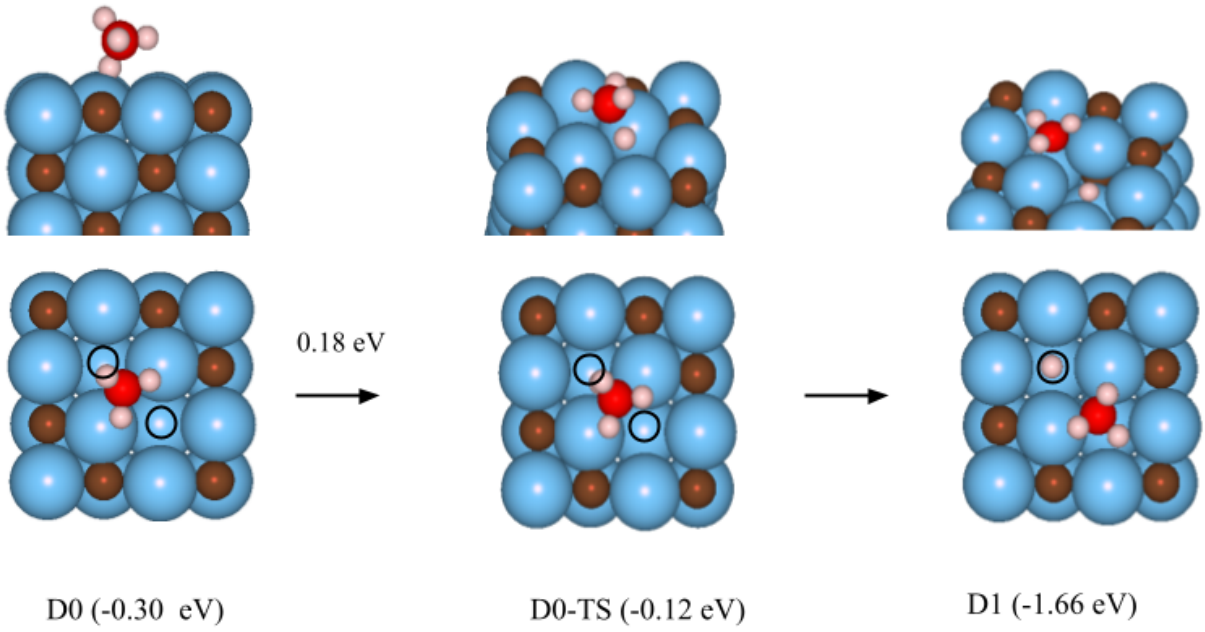

Figure 3.12: Side and top views of the reaction profile for $CH_4^\star$ (D0)$\rightarrow$ $CH_3^\star$+$H^\star$ (D1) on surface with divacancy. The energies in parenthesis represent the ZPE corrected energy of the state with respect to the gas phase energy of the CH_4 molecule and the energy of the clean slab.

3.5.4 $CH_3^\star$+$H^\star$ $\rightarrow$ $CH_2^\star$+2$H^\star$

The CH_3 group thus formed splits to form a CH_2 group and a H atom attached to a carbon atom on the surface (D2) in the final state (Fig. 3.13). The CH_2 group is located at a distance of 0.44 Å from the surface. The distance between the surface C and H atom formed from dissociation of the C-H bond is 1.13 Å. In the CH_2 moiety, the C-H bond pointing towards the vacancy is elongated to 1.16 Å while the one facing away from it has a bond length of 1.13 Å. This step corresponds to a reaction energy of -0.85 eV, and is more exothermic than the corresponding step for the single vacancy surface. The reaction proceeds through the formation of an intermediate (D1-I). The first transition state (D1-TS1) which forms the rate limiting step of the reaction, has an activation energy of 0.46 eV, and corresponds to the breaking of the longest C-H bond of $CH_3^\star$. The transition state leading from the intermediate to the most stable configuration of CH_2 on the surface corresponds to an activation energy of 0.16 eV. This transition state (D1-TS2) corresponds to the rotation of the CH_2 group.

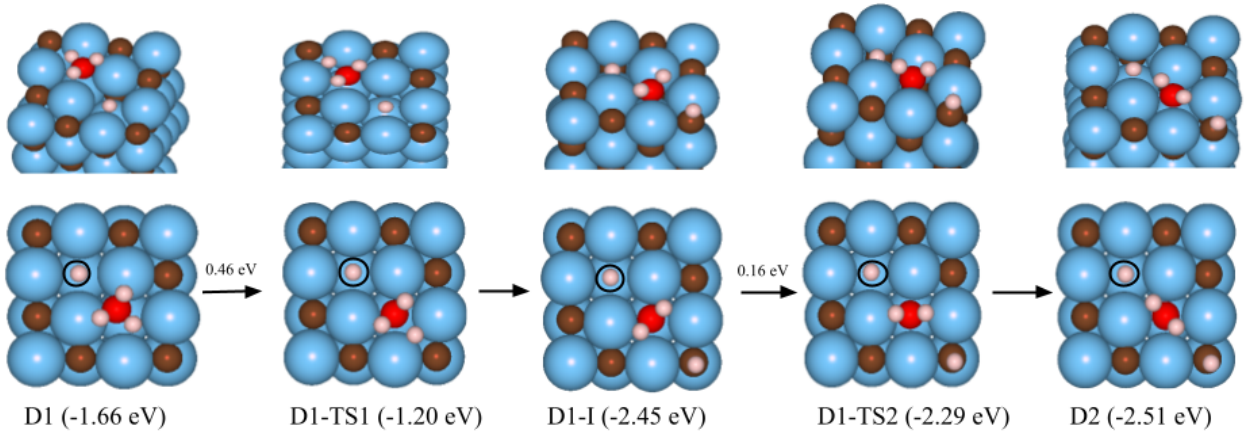

Figure 3.13: Side and top views of the reaction profile for $CH_3^\star$+$H^\star$ (D1)→ $CH_2^\star$+2$H^\star$ (D2) on surface with divacancy. The energies in parenthesis represent the ZPE corrected energy of the state with respect to the gas phase energy of the CH_4 molecule and the energy of the clean slab.

3.5.5 $CH_2^\star$+2$H^\star$ → $CH^\star$+3$H^\star$

The CH_2 group formed in the previous step can further dissociate to form a CH group and a H atom attached to one of the C atoms on the surface (Fig. 3.14). The longer C-H bond in the CH_2 moiety formed in the previous step, dissociates. The CH group thus formed is located at a distance of 0.26 Å from the surface, with a C-H bond length of 1.13 Å. The surface C-H distance for the H atom formed on dissociation of the CH_2 group is 1.13 Å. This step corresponds to a reaction energy of -0.42 eV. The step proceeds through the formation of an intermediate (D2-I) in which the H atom formed from dissociation of the C-H bond occupies the bridge site in between the two vacancies. The transition state leading to the intermediate (D2-TS1) has an activation energy of 0.30 eV and is the rate determining step for this reaction. D2-TS1 corresponds to the breaking of the C-H bond. The second transition state (D2-TS2) leading from the intermediate to the most stable configuration corresponds to an activation energy of 0.03 eV and is due to the diffusion of the H atom from the bridge site in D2-I to the top of one of the C atoms surrounding the vacancy.

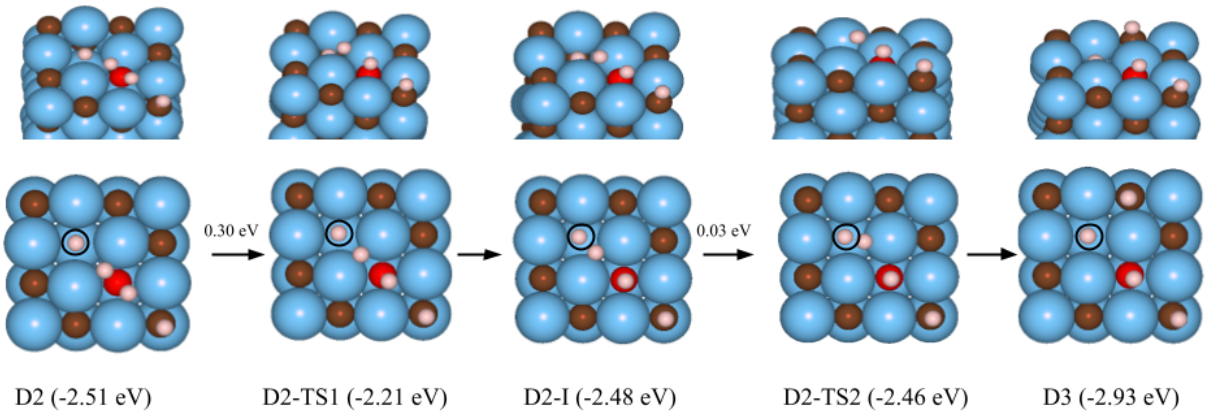

Figure 3.14: Side and top views of the reaction profile for $CH_2^\star$+2H* (D2)→ CH*+3H* (D3) on surface with divacancy. The energies in parenthesis represent the ZPE corrected energy of the state with respect to the gas phase energy of the CH_4 molecule and the energy of the clean slab.

3.5.6 CH*+3H* → C*+4H*

The final step in the reaction sequence for complete dissociation of $CH_4^\star$ → C* + 4H* corresponds to the dissociation the CH group into a C and H attached to the surface (D4 in Fig. 3.15). The C atom formed on dissociation occupies one of the defect sites. The H atom formed on dissociation occupies the top of one of the C atoms on the surface. The surface C-H distance is 1.13 Å. This step is only slightly exothermic with a reaction energy of -0.10 eV. The reaction proceeds through the formation of an intermediate (D3-I) where the H formed from dissociation of the C-H bond occupies the bridge site in between the defects. The first transition state (D3-TS1) with an activation energy of 0.49 eV corresponds to the splitting of the C-H bond. The second transition state (D3-TS2) leading from the intermediate to the final configuration corresponds to an activation energy of 0.17 eV and is due to the diffusion of the H atom from the bridge site to the carbon top. The final configuration (D4) is similar to the single defect surface with 3 H atoms occupying the surface C-tops and one H atom occupying the vacancy.

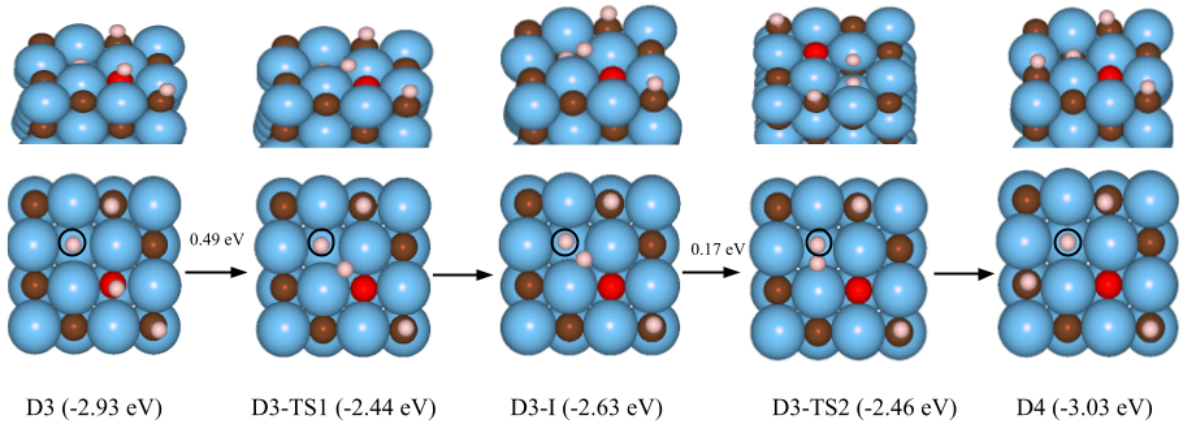

Figure 3.15: Side and top views of the reaction profile for $CH^{\star}+3H^{\star}$ (D3)$\rightarrow$ $C^{\star}+4H^{\star}$ (D4) on surface with divacancy. The energies in parenthesis represent the ZPE corrected energy of the state with respect to the gas phase energy of the CH_4 molecule and the energy of the clean slab.

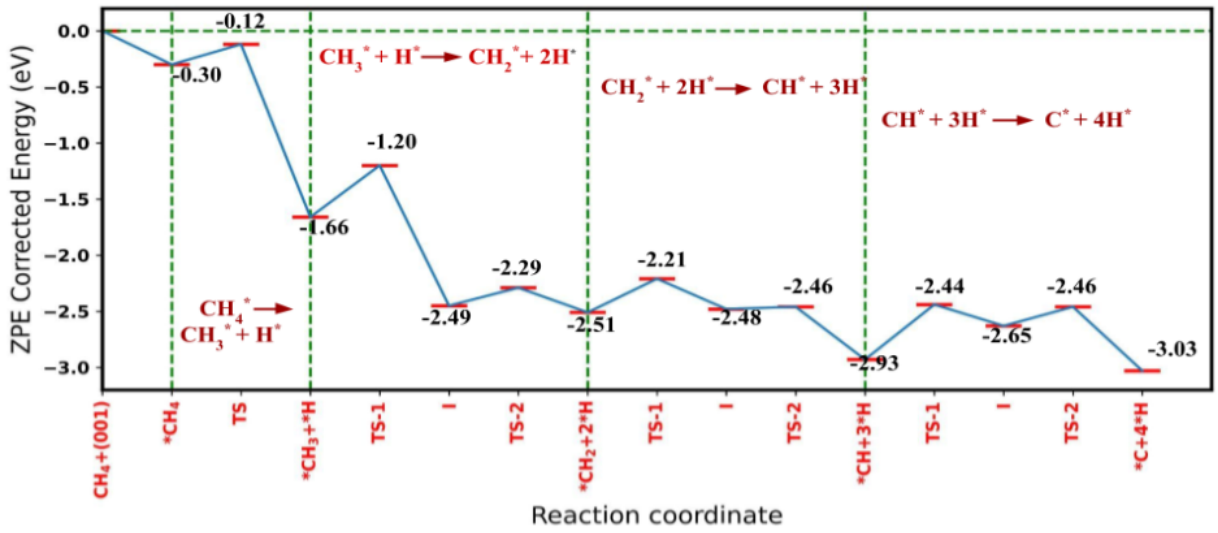

Figure 3.16: Complete Reaction profile for $CH_4^\star \rightarrow C^\star + 4H^\star$ on surface with divacancy. The energies represent the ZPE corrected energy of the state with respect to the gas phase energy of the CH_4 molecule and the energy of the clean slab.

Charge Analysis

The PDOS is calculated in order to understand the nature of the new states forming due to the overlap of the lowest unoccupied molecular orbitals (LUMO) of CH_4 molecule when it accepts electron density from the surface. The results are plotted (Fig. 3.17) in order to visualise the overlap of the CH_4 states with those of the surface. Minor overlap is observed between the C-2p, and H-s orbitals of the CH_4 molecule with the Ti-3d orbitals, particularly near the Fermi energy. This indicates that there is some charge transfer occurring from the surface to the CH_4 molecule around the Fermi energy, leading to a weakening or activation of the C-H bond. The ILDOS is calculated for these overlapping states around the Fermi energy. The states around the Fermi energy, in the range of 0.00-0.34 eV, have significant contributions from the Ti-3d orbitals from the surface Ti atoms and the two Ti atoms situated directly beneath the defect, and minor contributions from the methane C-H bond pointing towards the defect. The contribution to the DOS by the methane molecule around the Fermi energy has a predominantly C(2p) character.

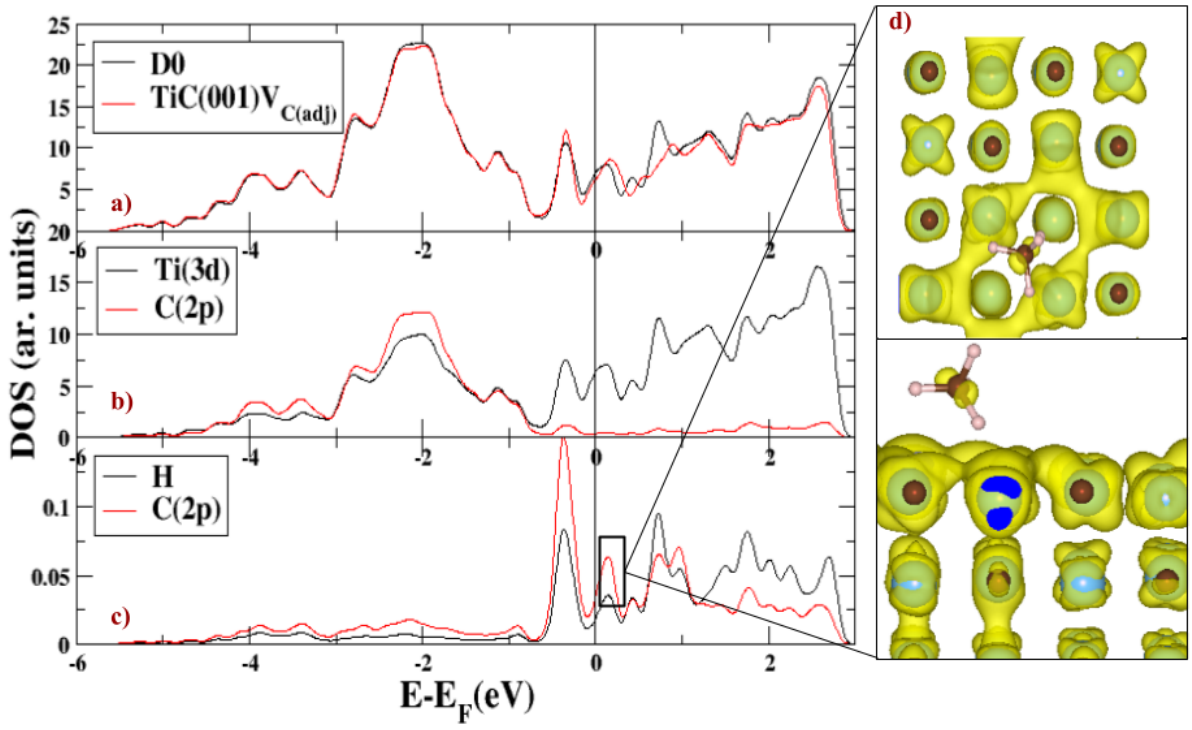

Figure 3.17: (a) DOS of molecule adsorbed on surface (D0) and free surface, (b) shows contributions of Ti(3d) and C(2p) orbitals to the DOS of D0, (c) shows contributions of C(2p) and H(1s) orbitals of the adsorbed CH_4 molecule. (d) ILDOS plot for CH_4 adsorption on divacancies at an isovalue of 0.0019, showing top and side views.

In order to understand the charge transfer from the surface to the CH_4 molecule the electron density difference between D0 and the clean surface and gas phase CH_4 molecule is plotted in Fig. 3.18a and Fig. 3.18b. The blue lobes represent regions of reduced charge density, and the yellow lobes represent regions of increased charge density. Regions of increased electron density are observed on the C atom of the CH_4 molecule, and regions of diminished charge density are observed on the Ti atoms surrounding the defect. This indicates that electron density is transferred from the surface Ti atoms to the CH_4 molecule leading to the activation of the C-H bond.

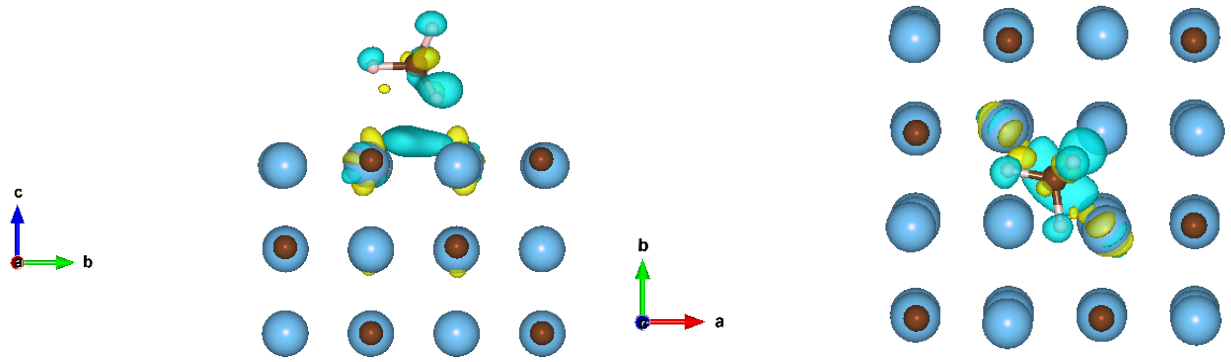

(a) Side View (b) Top View

Figure 3.18: Charge transfer isosurfaces for CH_4 adsorption on di-vacancies at an isovalue of 0.0013. Yellow lobes represent reduced charge density. Blue lobes represent increased charge density.

The charge transfer from the surface to the CH_4 molecule adsorbed on the divacancy is slightly greater (-0.08 e) compared to the single vacancy case (-0.07 e). The negative charge on the C atom of the CH_x group increases in magnitude as the C-H bonds dissociate sequentially, as tabulated in Table. 3.2. After complete dissociation the C from the CH_4 molecule occupies one of the vacancies on the surface. The charge on this C atom is similar to the charge on the other surface C atoms (-1.69 e). The charge on the H atom sequestered in the defect remains close to -0.60 throughout the C-H bond dissociation steps.

Table 3.2: Net Atomic Charges on the C of the $CH_x^\star$(x=0-4)

$CH_4^\star$	$CH_3^\star$+H*	$CH_2^\star$+2H*	CH*+3H*	C*+4H*
-0.61	-1.01	-1.28	-1.58	-1.69

3.5.7 Comparison of CH_4 activation on surfaces

We further compare the performance of the present catalyst with a wide range of other catalysts that has been reported in literature. The C-H bond cleavage activation energies on transition metal carbide and oxide surfaces, transition metal surfaces and small clusters supported on TMCs and TMs are presented in Table 3.3. We find that the barrier for CH_4 to CH_3 formation is comparable to the best candidates reported in literature. In particular we

can compare the C-H dissociation barriers to Ti_2C which is a similar carbide based catalyst. On Ti_2C there are 50% C-vacancies on the surface (in addition to interstitial C-vacancies) which provide active sites for CH_4 adsorbtion and dissociation. However, on Ti_2C, CH_4 dissociation is facile, and elemental C is readily formed on the surface. This poisons the catalyst surface, and renders it unusable for repeated catalytic cycles. On the single vacancy TiC(001) surface (12.5% C-vacancy) the C-H bond dissociation barriers increase gradually following the first C-H activation. This implies that CH_4 dissociation is not facile on this surface. In contrast, on the divacancy containing TiC(001) surface (25% C-vacancy) again the CH_4 dissociation is facile. For the single vacancy case, since the activation energies of the subsequent C-H bond cleavage are higher than the best candidates reported in literature, we anticipate that this might be a good candidate where there will be control on the bond cleavage and can be used for selectively making other products. In particular, in the subsequent sections, we present our results for C-C coupling reactions on the single vacancy surface.

Table 3.3: Comparison of the energy barriers (reported in eV, ZPE corrected) of CH_x (x= 1–4) cleavage

Surfaces	$CH_4^\star \rightarrow CH_3^\star + H^\star$	$CH_3^\star + H^\star \rightarrow CH_2^\star + 2H^\star$	$CH_2^\star + 2H^\star \rightarrow CH^\star + 3H^\star$	$CH^\star + 3H^\star \rightarrow C^\star + 4H^\star$
Oxide/carbide surfaces				
Single vacancy (TiC(001))	0.24	0.73	0.89	1.69
Di-vacancy (TiC(001))	0.18	0.46	0.30	0.49
Ti_2C[9]	0.22 (0.19)	0.03 (0.06)	0.14 (0.13)	0.61 (0.63)
TiC(001)[9]	1.22	-	-	-
α-MoC(001)[6]	0.74	0.95	0.55	1.17
δ-MoC(111)[6]	0.49	0.50	0.33	1.10
IrO_2(110)[47]	0.25	0.61	1.15	0.62
Transition metal surfaces				
Cu(111)[48]	1.31	1.26	0.93	1.97
Pt(111)[48]	0.93	0.75	0.17	1.24
Pd(111)[49]	0.99	0.85	0.24	1.30
Ni(111)[50]	0.65	0.64	0.31	1.29
Pd(211)[50]	0.94	0.59	0.51	1.18
Large transition metal clusters				
Pt_{79}[49]	0.33	0.34	0.58	1.03
Pd_{79}[50]	0.57	0.61	0.37	0.95
Pd_{140}[50]	0.68	0.64	0.35	0.97
Small transition metal clusters on a support				
Ni_4/TiC(001)[8]	0.18	-	-	-
Mo_6C_4/Au(111)[15]	0.08	-	-	-
$Mo_{10}C_{12}$/Au(111)[15]	0.58	-	-	-

3.6 C-C coupling on single vacancy surface

Based on the results of CH_4 dissociation, we have studied C-C coupling reactions to form C_2 products on the TiC(001) surface with the single vacancy. In particular, we have focused on formation of three important compounds, namely, ethane (C_2H_6), ethylene (C_2H_4) and acetylene (C_2H_2) from coupling of CH_3, CH_2 and CH species, respectively, that are formed on the surface after the first, second and third C-H bond dissociation. On the surface containing the single vacancy, we observe that the CH_x species are bound closer to the vacancy, while the vacancy is blocked by the dissociated H. Hence, we anticipate that the C_2 products will be formed on the defect free part of the surface. The full reaction can be divided into two parts: (a) formation of C_2 products and their desorption and (b) regeneration of the catalyst through H_2 formation and desorption.

3.6.1 C_2 formation

In order to study the plausibility of C_2 formation on this surface, we considered the following mechanism: (i) the CH_x species bound close to the vacancy diffuses towards the defect free part of the surface, (ii) two diffusing CH_x species on the defect free part of the surface couples to form a C_2 product and (iii) desorption of the C_2 product from the surface. This is schematically shown in Fig. 3.19.

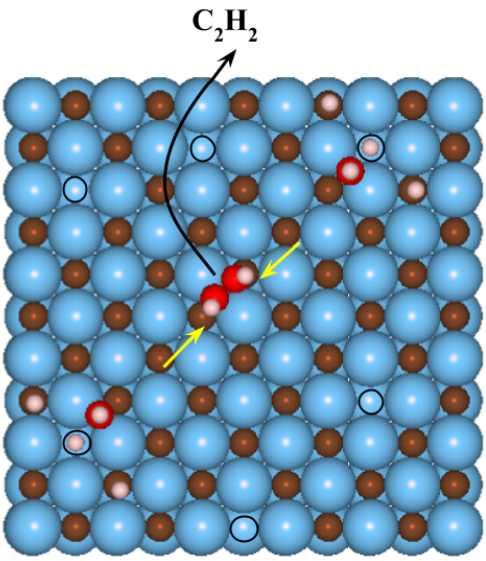

Figure 3.19: Schematic for C_2 coupling

CH_x diffusion: Diffusion of the CH_x species on the surface is an activated process. Further, the barriers associated with the diffusion near the vacancies might be different from that on the pristine surface, away from the vacancy. Hence, we have considered both the scenarios in our calculations. The results are summarized in Table 3.4. The detailed pathway is presented in Sec. 5.1, Sec. 5.2 and Sec. 5.3 of the Appendix. Amongst the CH_x species, CH_3 has the largest diffusion barriers. Their magnitude, both near and away from the vacancy are similar, suggesting that the vacancies does not influence the mobility of these species on the surface. In contrast, for CH_2, the diffusion barrier on the defect free part of the surface is less than half of that observed near the C-vacancy (1.39 eV near the vacancy vs 0.63 eV away from the vacancy). Interestingly, our calculations show that for the CH species, the diffusion barrier in presence of the C-vacancy is about 0.25 eV lower than that observed on the defect free part of the surface. Overall, amongst the three CH_x species, CH is the most mobile one.

Table 3.4: Comparison of migration vs dissociation barriers for CH_x (a=ZPE corrected)

Species	C-H dissociation barrier(eV)	Diffusion barrier near vacancy (eV)	Diffusion barrier on defect-free surface (eV)
CH_3	0.73	1.64	1.61
CH_2	0.89	1.39	0.63
CH	1.69[a]	0.43[a]	0.68[a]

3.6.2 CH coupling to form C_2H_2

In this step the two diffusing CH groups come together and couple on the surface, away from the vacancies, to form C_2H_2. The reaction profile is depicted in Fig. 3.20. In the starting configuration (C1) two CH groups are adsorbed at adjacent diagonal Ti-Ti bridge site. In the final configuration (C2) when C_2H_2 is formed, the acetylene molecule is adsorbed on a diagonal C-C bridge site, with the C-C bond almost parallel to the surface. The C-C bond length in $C_2H_2^\star$ is 1.45 Å compared to a C-C bond length of 1.20Å in gaseous C_2H_2. The reaction energy for $2CH^\star \rightarrow C_2H_2^\star$ is -1.53 eV, indicating that the reaction is thermodynamically favourable. The reaction proceeds through two intermediates. In the first intermediate (C1-I1), which is 0.23 eV higher in energy compared to C1, one of the CH groups migrates onto the C-Ti bridge. This step corresponds to an activation energy of 0.49 eV. This is followed by the migration of the other CH group onto a C-Ti bridge to form the second intermediate (C1-I2). This step has an activation energy of 0.67 eV. The intermediate formed at the end of this step is 0.62 eV uphill compared to the starting configuration. In this intermediate both the CH groups occupy C-Ti bridges. The final transition step (C1-TS3) corresponds to the coupling of these CH groups to form an ethyne molecule. This process has an activation energy of 0.03 eV. The non-ZPE corrected desorption energy of C_2H_2 from defect free surface is 3.44 eV. In the vicinity of the vacancy however the desorption energy of C_2H_2 is only 2.54 eV. The presence of adsorbed H atoms in and around the vacancy sterically hinders C_2H_2 adsorption and leads to weaker binding and as a result easier desorption of the C_2H_2 molecule from the surface.

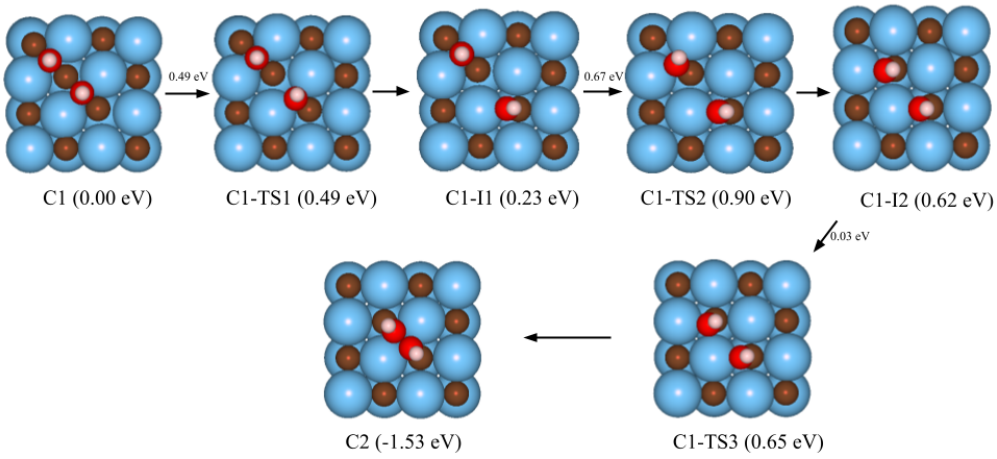

Figure 3.20: Top views of the reaction profile for $C_2H_2^\star$ formation on the defect-free surface. The energies in parenthesis are the ZPE corrected energies with respect to the initial state C-1.

3.6.3 Catalyst regeneration

Once C_2H_2 desorbs, we are left with the surface containing H atoms. Some of the H atoms are bound to the defect free part of the surface while others occupy the C-vacancy. Hence to continue with the catalytic cycle it is necessary to desorb the H atoms to free up the C-vacancies that act as adsorption site for the next incoming methane molecule. Therefore, in this section we explore the regeneration of catalyst through H_2 formation.

Post acetylene formation, each methane molecule leaves behind three H atoms, two of which are adsorbed on top of the C-atoms surrounding the defect, while the third one occupies the defect site. Several reaction sequences may lead to the removal of H atoms, including (a) the combination of the H atom in the vacancy with one of the H atoms on the surface to produce H_2, which then desorbs and regenerates the vacancy, and (b) the migration of an H atom away from the vacancy to the defect-free surface, followed by two possible scenarios - (c1) the slipping of the third H atom into the defect to combine with an H atom that has migrated away from another defect, resulting in the formation of an H_2 molecule, or (c2) the combination of two H atoms on the defect-free part of the surface to create an H_2 molecule. Based on the activation barriers for these possible mechanisms, possibilities (a) followed by steps (b) and (c1) are observed to be more feasible and are discussed in detail. Possibility (c2) has been explored in more detail in Sec. 5.4 of the Appendix.

(a) Vacancy Regeneration

The H atom on the surface that is closer to the H atom in the vacancy is expected to combine with it to form an H_2 molecule. The starting configuration is H1 (Fig. 3.21). Post recombination, the H_2 molecule formed is adsorbed on top of the Ti atom surrounding the defect (H2) as shown in Fig. 3.21. The whole reaction is thermodynamically uphill with a reaction energy of 1.53 eV. It proceeds through an intermediate (H1-I) in which the H atom occupying the C-top in H1 moves to the Ti-Ti bridge site next to the defect. This intermediate is 0.53 eV uphill compared to the initial configuration. The transition state (H1-TS1) leading up to this intermediate corresponds to an activation energy of 0.61 eV. The second part of the reaction corresponds to pulling the H atom away from the vacancy, and the coupling of this H atom to the H atom that has previously moved onto the Ti-Ti bridge in the intermediate configuration, to form an H_2 molecule. This step corresponds to an activation energy of 0.99 eV. The transition state leading up to the final state (H1-TS2) corresponds to moving the H atom out of the vacancy. The reaction steps are depicted in Fig. 3.21. An energy of 0.24 eV is required to desorb the H_2 molecule formed in the H2 configuration.

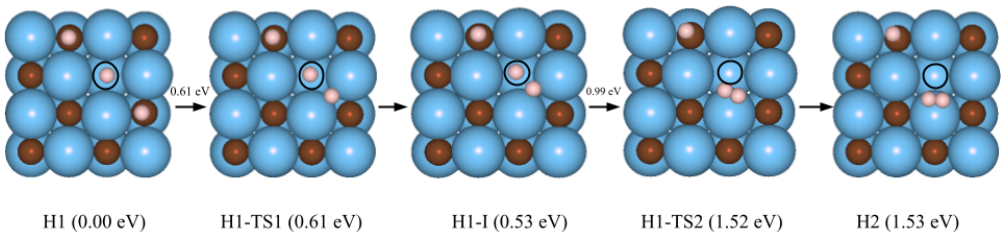

Figure 3.21: Top views of the reaction profile for $H_2^\star$ formation on the at the vacancy. The energies in parenthesis are the ZPE corrected energies with respect to the initial state H1.

(b) H atom migration near vacancy and on defect-free surface

H migration near the vacancy (depicted in Fig. 3.22) corresponds to a reaction energy of 0.07 eV. The transition state corresponds to an activation energy of 0.98 eV. In the transition state the H atom occupies a Ti-Ti bridge.

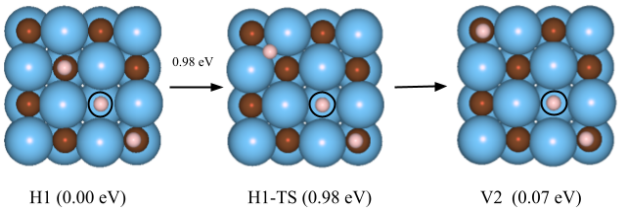

Figure 3.22: Top views of the reaction profile for H migration near the vacancy. The energies in parenthesis are the ZPE corrected energies with respect to the initial state H1.

H migration on the defect-free surface corresponds to an activation energy of 0.98 eV. The structure of the transition state (P1-TS) in this case is similar to the transition state structure for H migration near the vacancy. The reaction profile for H migration on the defect-free surface is depicted in Fig. 3.23.

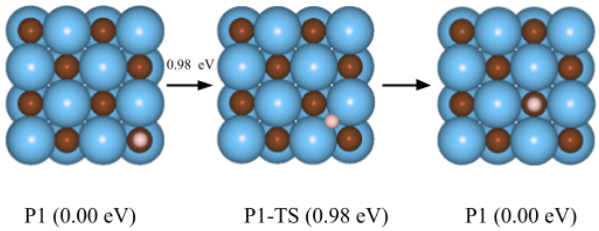

Figure 3.23: Top view of the reaction profile for H* migration on the defect-free surface. The energies in parenthesis are the ZPE corrected energies with respect to the initial state P1.

(c1) H atom reoccupying the vacancy followed by H_2 evolution

In this scenario we consider the sequence of steps that could occur after the H_2 molecule formed in case (a) desorbs from the surface. The H atom that was previously adsorbed on the C atom surrounding the vacancy can slip into the regenerated vacancy. This step corresponds to an activation energy of 0.49 eV for the transition state Q1-TS and a reaction energy of -0.76 eV leading to the final configuration Q2. The reaction is depicted in Fig. 3.24.

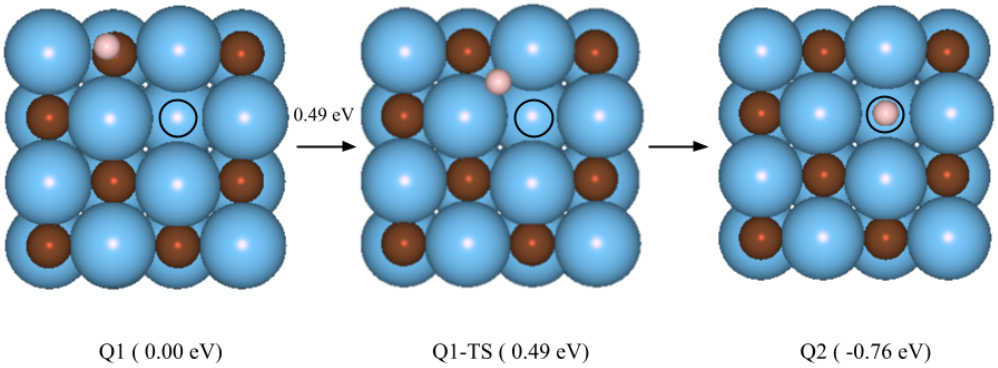

Figure 3.24: H atom reoccupying the vacancy

Once the third H atom on the surface reoccupies the defect, it is expected that another H atom will migrate from another defect on the surface and couple with this H atom inside the defect leading to the formation of an H_2 molecule, and the regeneration of the vacancy. This reaction (depicted in Fig. 3.25) proceeds through an intermediate (G1-I) in which the H atom on the C top occupies a Ti-Ti bridge. The first transition state (G1-TS1) leading up to the intermediate requires an activation energy of 0.77 eV and the second transition state (G1-TS2) which involves pulling the H atom out of the defect corresponds to an activation energy of 0.87 eV.

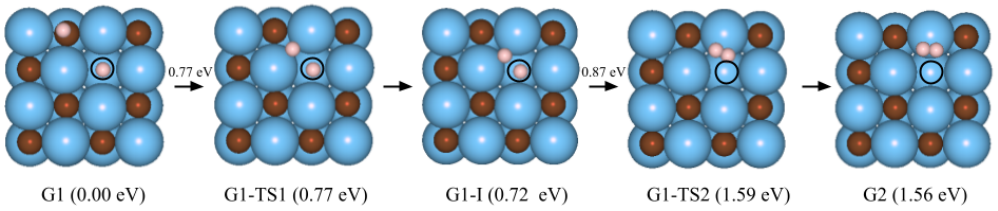

Figure 3.25: H_2 evolution at the vacancy after vacancy reoccupation

The activation energy required for 2 H atoms to combine on the pristine surface is 1.83 eV (Sec 5.4 of Appendix). The activation energy required for the third H atom to slip into the defect is only 0.49 eV, making the vacancy reoccupation the more favoured process. Subsequent H_2 evolution at the vacancy also has significantly lower activation energies compared to H_2 formation on the defect-free surface.

The high activation energy for the 2 H atoms to combine on the defect free surface makes (c2) the least probable mechanism for H_2 evolution from the surface.

3.7 Temperature dependence of energetics

The Gibbs free energies for all reaction steps are calculated across a range of temperatures to understand the impact of temperature on the reaction (discussed in more detail in Sec. 5.5 of the Appendix).

As temperature increases on the single vacancy surface, the activation energy for initial C-H bond activation also increases, but the activation energies for subsequent C-H bond dissociation steps decrease. Meanwhile, for the 2 CH groups, higher temperatures result in lower diffusion barriers, and as a result, increased mobility on both defect-containing and defect-free surfaces. At elevated temperatures, the formation and removal of C_2H_2 is more likely due to lowered free energy of formation and lower C_2H_2 desorption energies, respectively. Similarly, higher temperatures make vacancy regeneration, H migration on defect-containing and defect-free surfaces, and H_2 evolution at the defect more feasible by lowering the energy barriers.

At an optimal temperature, the CH_4 molecule adsorption and activation should be feasible on the single vacancy, the last C-H dissociation barrier to form $C^{\star}$+4$H^{\star}$ should be high enough such that complete dissociation of CH_4 is not facile, the CH migration, CH coupling, C_2H_2 desorption, H migration and H_2 formation should be feasible. According to the free energy analysis, at 600 K, the formation of $CH^{\star}$ from CH_4 is facile, with the largest free energy barrier of 0.75 eV for CH^{*} formation from CH_2^{*} but the formation of C+4H is not (activation free energy of 1.52 eV). The competing CH migration barriers near the vacancy and on the defect-free surface are 0.37 eV and 0.60 eV, respectively, suggesting that it will be more probable for the CH species to diffuse on the surface, meet each other and form C_2H_2 rather than undergoing further dissociation that will lead to coke formation. This is further supported by the fact that the rate-determining free energy barrier for the formation of C_2H_2 is 0.38 eV, with a reaction free energy of -1.51 eV. At 600 K, the H diffusion barriers near the vacancy and on the defect-free part of the surface are both 0.87 eV. The rate-determining free energy barrier at 600 K for H_2 evolution at the vacancy is 0.85 eV. Amongst the different competing processes for the non-oxidative coupling of methane to form acetylene, the rate limiting step is the desorption of C_2H_2 on the surface with a desorption free energy of 2.34 eV. However, we note that these values are computed for the clean surface. We envisage that under realistic reaction conditions, the surface will be covered with H. Therefore, in presence of H, the desorption free energy is lowered due to the weakening of acetylene adsorption

strength on the surface, which is caused by steric repulsion between C_2H_2 and H. Presently, the calculations for the temperature dependence of this step are going on.

Chapter 4

Conclusion

In this thesis we have studied the activation of CH_4 on TiC(001) surfaces containing 12.5% (single vacancy) and 25% C-vacancies (divacancy). In order to understand the reactivity of the surfaces we have studied the complete dissociation of CH_4 on these surfaces. Both the single and divacancy containing surfaces are able to adsorb and activate CH_4. On the former the first C-H bond activation is feasible, however the subsequent C-H bond dissociation barriers increase gradually. The last C-H bond dissociation leading to the complete dissociation of methane into C + 4 H is unlikely because of the very high activation energy associated with this step. For the surface containing 25% C-vacancies, the CH_4 activation process is easier compared to the single vacancy and the subsequent C-H bond dissociations have low activation barriers and exothermic reaction energies. The facile nature of C-H dissociations leads to surface poisoning due to the formation of a C atom in one of the 2 C vacancies on the surface, thereby making catalyst regeneration difficult. These observations lead us to the conclusion that the concentration of C-vacancies affects the reactivity of the TiC(001) surface for CH_4 activation.

Based on these observations we can also conclude that the divacancy surface is not well suited for partial CH_4 activation, which is required in order to obtain methane derivatives. The single vacancy surface on the other hand has the potential to act as a catalyst for the direct conversion of methane into valuable products. From the analysis of the CH_x species diffusion barriers, we find that CH diffusion on the surface is not only more feasible compared to CH_2 or CH_3 diffusion but also more facile compared to further C-H bond cleavage. The

CH groups couple on the defect-free part of the surface away from the vacancy, leading to the formation of C_2H_2. C_2H_2 formation on the TiC(001) surface has low barriers and the reaction is more exothermic than C-C coupling observed on similar metal carbide catalysts such as Mo_2C,[6] Ti_2C[9] and WC.[7]

For a catalyst to be economically viable it must be able to sustain repeated catalytic cycles without losing its reactivity. On this catalyst, the C-vacancies are the active sites for the CH_4 activation reaction which should be regenerated after every catalytic cycle in order to maintain the reactivity of the catalyst. Therefore, we have explored the regeneration of the catalyst following the formation and desorption of the C_2 product. Catalyst regeneration involves removal of the H atoms from the surface in the form of H_2. We have also studied the effect of temperature on the reaction. We observe that high temperatures enable easier formation and desorption of C_2H_2 from the surface. The ease of C-H activation and the selectivity of the single C-vacancy containing TiC(001) surface towards methane dissociation, as well as the feasibility of C-C coupling on this surface makes the single vacancy TiC(001) surface a promising catalyst for methane activation and C_2 coupling reactions.

Chapter 5

Appendix

5.1 CH_3 diffusion

The CH_3 species is adsorbed on top of one of the carbon atom surrounding the defect. Initially, we study the migration of CH_3 near the defect (Fig. 5.1). Various possible configurations for CH_3 adsorption away from the defect are considered, on both C and Ti tops. The C-top configurations are more stable than the Ti top configurations. In the most stable adsorption geometry of CH_3 away from the vacancy (S1-1), the CH_3 group adsorbs over the C-atom located one C-atom diagonally across the defect. This migration corresponds to an endothermic reaction energy of 0.21 eV, and an activation energy of 1.64 eV. The transition state (S1-TS) corresponds to the breaking of the C-C bond in which the CH_3 group occupies the Ti-Ti bridge position.

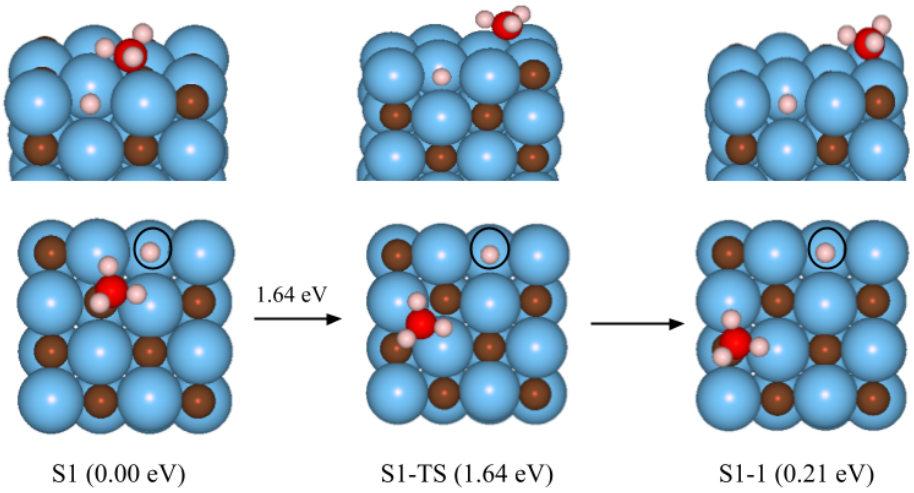

Figure 5.1: Side and top views for reaction profile for $CH_3^\star$ migration near the vacancy. The energies in parenthesis are the non-ZPE corrected energies with respect to the initial state S1.

The diffusion of the CH_3 group on the pristine surface has initial and final states of a similar geometry (M1). The diffusion barrier on the pristine surface is 1.61 eV and occurs through a state (M1-TS) in which the CH_3 group occupies the Ti-Ti bridge. The geometry of M1-TS in this case is similar to that of S1-TS in the vicinity of the vacancy. The reaction profile is represented in Fig. 5.2.

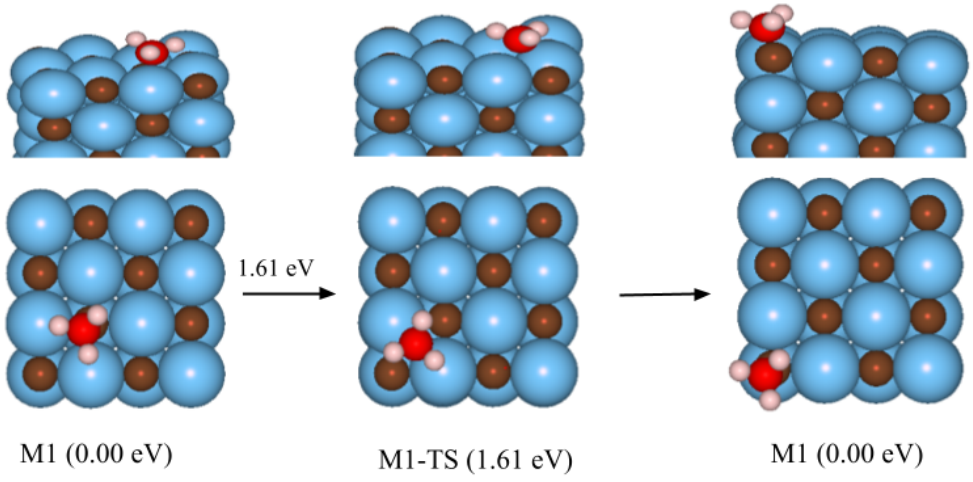

Figure 5.2: Side and top views for reaction profile for $CH_3^\star$ migration on defect-free surface. The energies in parenthesis are the non-ZPE corrected energies with respect to the initial state M1.

The resemblance of M1-TS and S1-TS structures and the diffusion barrier in the vicinity of the vacancy vs further away from it on the defect-free surface implies that the vacancy does not play an important role in the diffusion of the CH_3 group. This could be due to the fact that the splitting of the first C-H bond does not alter the surface appreciably. Only the H-atom occupies the defect, the Ti and C atoms on the surface away from the defect are practically unchanged. However the diffusion barrier for CH_3 is higher than the activation barrier for the dissociation of the C-H bond in CH_3 that leads to the formation of CH_2 (0.86 eV). Hence, it is unlikely that CH_3 diffuses on the surface. The more probable step after the dissociation of the first C-H bond is the dissociation of the second C-H bond to form a CH_2 group adsorbed on the surface.

5.2 CH_2 diffusion

After the CH_2 group is formed, as in the above case, it could either migrate to the defect-free surface to couple with another CH_2 group to form C_2H_4, or one of the C-H bonds could dissociate leading to the formation of a C-H group. As before, the barriers for CH_2 migration are calculated, near the vacancy and away from it. Near the vacancy, CH_2 migration has an activation energy of 1.39 eV and an endothermic reaction energy of 0.46 eV. In the TS, the CH_2 group occupying the Ti-Ti bridge, and the TS is formed due to the breaking of the C-C bond. In the final configuration the CH_2 group occupies the C-atom placed diagonally one C away from the vacancy (S2-1). The migration profile is depicted in Fig. 5.3.

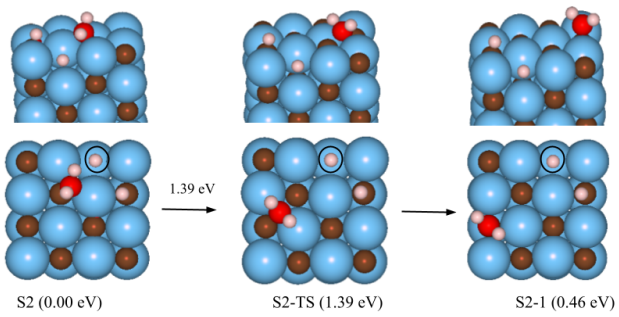

Figure 5.3: Side and top views for reaction profile for $CH_2^\star$ migration near the vacancy. The energies in parenthesis are the non-ZPE corrected energies with respect to the initial state S2.

The final CH_2 adsorption geometry is similar to CH_2 adsorption geometry on the pristine surface (M2). On the defect-free surface, away from the vacancy, the CH_2 migration has an activation barrier of 0.63 eV. The M2-TS geometry is similar to the one observed in the neighbourhood of the vacancy, with the CH_2 group occupying the Ti-Ti bridge (Fig. 5.4).

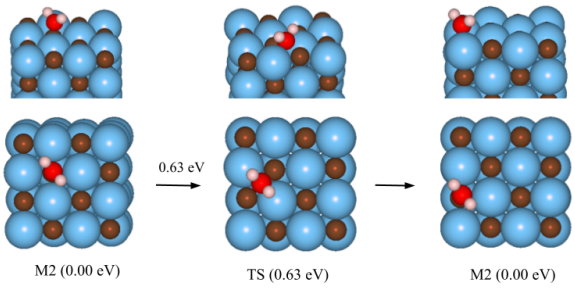

Figure 5.4: Side and top views for reaction profile for $CH_2^\star$ migration on defect-free surface. The energies in parenthesis are the non-ZPE corrected energies with respect to the initial state M2.

For CH_2, diffusion barriers vary greatly near the vacancy and on the defect-free surface.

This could be due to the repulsive interactions of the CH_2 group with the H atoms adsorbed on the surface near the vacancy. The CH_2 diffusion barrier near the vacancy is also higher than the activation of the third C-H bond to form CH from CH_2, which has an activation energy of 1.01 eV. Therefore, the more probable step after the dissociation of the second C-H bond is the dissociation of the third C-H bond to form a CH group adsorbed on the surface.

5.3 CH diffusion

The CH_2 produced preferentially dissociates to form CH on the surface. The CH group thus formed can migrate away from the vacancy onto the defect-free surface, where it could react with another CH group to form C_2H_2. Based on the migration barriers and the bond dissociation barriers reported above the migration of CH groups seems more favourable.

CH migration away from the vacancy proceeds through a rate determining step (S3-TS1) corresponding to an activation energy of 0.43 eV. In the intermediate state (S3-I) the CH group occupies the C-Ti bridge. The intermediate is 0.39 eV uphill with respect to the starting configuration. The second transition state (S3-TS2) corresponds to an activation energy of 0.37 eV. The final configuration for the CH group away from the vacancy (S3-1) is 0.33 eV uphill compared to the most stable $CH^\star$ configuration on the surface adjacent to the vacancy. The initial and final states for CH diffusion near the vacancy is depicted in Fig. 5.5.

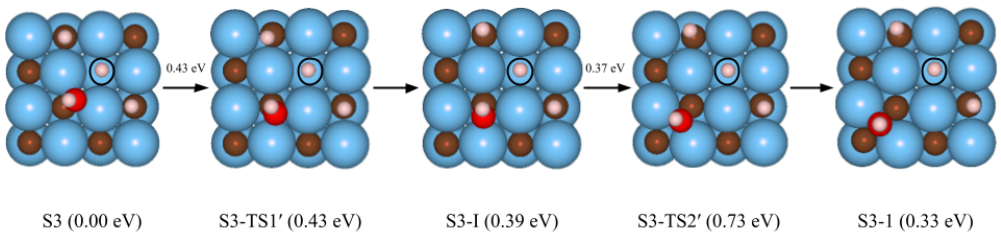

Figure 5.5: Top views for the initial and final states for $CH^\star$ migration near the vacancy. The energies in parenthesis are the ZPE corrected energies with respect to the initial state S3.

On the defect-free surface the most favoured configuration for CH adsorption is at the

bridge site in between two Ti and two C atoms. The migration of CH from one bridge position to the next occurs through an intermediate (M3-I) in which the CH group is situated at the C-Ti bridge. This intermediate is 0.52 eV uphill relative to the starting configuration (M3). The reaction pathway from the intermediate (M3-I) to the final state is symmetric to the path from the initial state to the intermediate, since the initial and final configurations are equivalent. The first transition state (M3-TS1) corresponds to an activation energy of 0.68 eV, whereas the second transition state (M3-TS2) corresponds to an activation energy of 0.16 eV. The initial and final states for CH diffusion on the defect-free surface is depicted in Fig. 5.6.

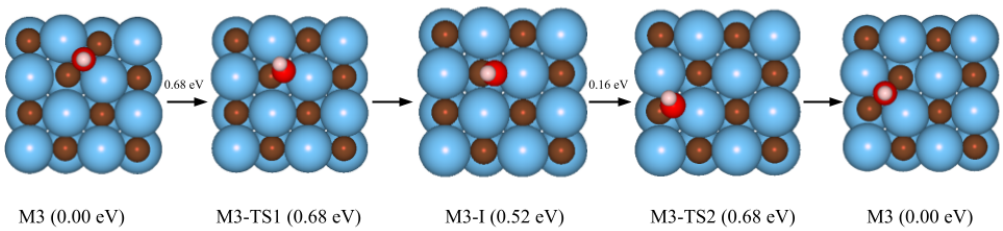

Figure 5.6: Side and top views for the initial and final states for CH* migration on the defect-free surface. The energies in parenthesis are the ZPE corrected energies with respect to the initial state M3.

5.4 H_2 evolution on defect-free surface

On the defect-free surface two H atoms are adsorbed on diagonally situated C tops as in R1 (Fig. 5.7). The transition state (R1-TS) corresponds to one of the H atoms translating on top the Ti atom adjacent to the other Ti atom. These two H atoms eventually couple to form a H_2 molecule. In the final state (R2) the H_2 molecule is adsorbed on top of a surface Ti atom, parallel to the surface. This reaction step is endothermic corresponding to a reaction energy of 1.04 eV. The activation energy for this step is 1.82 eV.

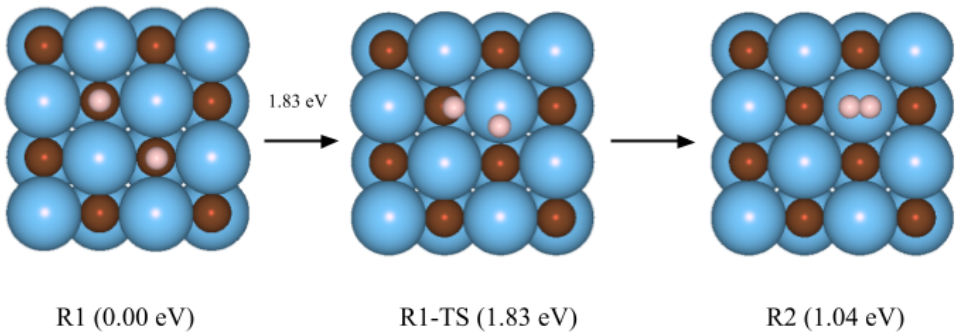

Figure 5.7: Top views for the initial and final states for H_2 evolution on the pristine surface. The energies in parenthesis are the ZPE corrected energies with respect to the initial state R1.

5.5 Temperature dependence

5.5.1 Single vacancy

Table 5.1: Free energies of activation (in eV) of C-H bond with respect to temperature.

T(K)	$CH_4^\star \rightarrow CH_3^\star + H^\star$ TS-1	$CH_4^\star \rightarrow CH_3^\star + H^\star$ TS-2	$CH_3^\star + H^\star \rightarrow CH_2^\star + 2H^\star$	$CH_2^\star + 2H^\star \rightarrow CH^\star + 3H^\star$	$CH^\star + 3H^\star \rightarrow C^\star + 4H^\star$
DFT	0.39	0.40	0.86	1.02	1.82
0	0.24	0.39	0.73	0.89	1.69
298.15	0.29	0.38	0.67	0.83	1.62
400	0.32	0.37	0.65	0.80	1.59
600	0.35	0.35	0.60	0.75	1.52
1000	0.41	0.31	0.48	0.62	1.39
1200	0.44	0.29	0.42	0.55	1.32

Table 5.2: Reaction free energy (in eV) for C-H bond dissociation with respect to temperature

T(K)	$CH_4^\star \rightarrow CH_3^\star + H^\star$	$CH_3^\star + H^\star \rightarrow CH_2^\star + 2H^\star$	$CH_2^\star + 2H^\star \rightarrow CH^\star + 3H^\star$	$CH^\star + 3H^\star \rightarrow C^\star + 4H^\star$
DFT	-0.96	-0.01	0.29	0.77
0	-1.03	-0.09	0.13	0.75
298.15	-0.88	-0.10	0.10	0.73
400	-0.81	-0.11	0.08	0.73
600	-0.66	-0.13	-0.04	0.72
1000	-0.38	-0.19	-0.06	0.70
1200	-0.24	-0.22	-0.11	0.69

Table 5.3: Gibbs free energies of intermediates with respect to temperature (in K)

Intermediate	298.15	400	600	1000	1200
S0	0.06	0.16	0.35	0.69	0.85
S1	-0.82	-0.65	-0.32	0.31	0.61
S2	-0.92	-0.76	-0.45	0.12	0.39
S3	-0.82	-0.68	-0.41	0.06	0.27
S4	-0.09	0.05	0.31	0.76	0.96

5.5.2 Divacancy

Table 5.4: Free energy barriers (in eV) for C-H bond dissociation with respect to temperature.

T (K)	$CH_4^\star \rightarrow CH_3^\star + H^\star$	$CH_3^\star + H^\star \rightarrow CH_2^\star + 2H^\star$	$CH_2^\star + 2H^\star \rightarrow CH^\star + 3H^\star$	$CH^\star + 3H^\star \rightarrow C^\star + 4H^\star$
DFT	0.37	0.56	0.42	0.52
0	0.18	0.46	0.30	0.49
298.15	0.15	0.41	0.19	0.50
400	0.14	0.39	0.17	0.51
600	0.10	0.35	0.09	0.53
1000	0.03	0.27	-0.03	0.58
1200	-0.01	0.23	-0.05	0.59

Table 5.5: Reaction free energy (in eV) for C-H bond dissociation with respect to temperature.

T (K)	$CH_4^\star \rightarrow CH_3^\star + H^\star$	$CH_3^\star + H^\star \rightarrow CH_2^\star + 2H^\star$	$CH_2^\star + 2H^\star \rightarrow CH^\star + 3H^\star$	$CH^\star + 3H^\star \rightarrow C^\star + 4H^\star$
DFT	-1.18	-0.79	-0.29	-0.09
0	-1.36	-0.85	-0.42	-0.10
298.15	-1.30	-0.82	-0.49	-0.10
400	-1.27	-0.81	-0.54	-0.11
600	-1.22	-0.77	-0.65	-0.11
1000	-1.14	-0.72	-0.87	-0.12
1200	-1.11	-0.70	-0.98	-0.13

5.5.3 CH migration near vacancy

Table 5.6: Activation barrier (in eV) and reaction Energies (in eV) for CH migration on near the vacancy with respect to temperature.

T (K)	Activation barrier for TS-1 (eV)	Activation barrier for TS-2 (eV)	Reaction energy (eV)
DFT	0.46	0.41	0.30
0	0.43	0.37	0.33
298.15	0.41	0.34	0.35
400	0.39	0.32	0.36
600	0.37	0.28	0.39
1000	0.32	0.20	0.44
1200	0.29	0.17	0.47

5.5.4 CH migration on defect-free surface

Table 5.7: Free energy of activation (in eV) for CH migration on defect-free surface with respect to temperature.

T (K)	Activation barrier for TS-1 (eV)	Activation barrier for TS-2 (eV)
DFT	0.74	0.18
0	0.68	0.17
298.15	0.65	0.15
400	0.64	0.15
600	0.60	0.13
1000	0.52	0.10
1200	0.48	0.09

Since the initial and final states for CH migration on the pristine surface are identical, there is no reaction energy associated with this step.

Table 5.8: Free energy of intermediate (with respect to starting configuration, in eV) for CH migration on defect-free surface with respect to temperature.

T (K)	Free energy of intermediate (eV)
DFT	0.56
0	0.52
298.15	0.50
400	0.49
600	0.47
1000	0.42
1200	0.39

5.5.5 C_2H_2 formation and desorption

Table 5.9: Free energy (in eV) for C_2H_2 formation and desorption with respect to temperature.

T (K)	Reaction energy (eV)	Desorption energy (Defect-free surface) (eV)	Desorption energy (Near vacancy) (eV)
DFT	-1.59	4.07	3.09
0	-1.53	3.44	2.54
298.15	-1.52	2.94	2.02
400	-1.52	2.74	1.81
600	-1.51	2.34	1.39
1000	-1.47	1.53	0.55
1200	-1.46	1.14	0.14

Table 5.10: Free energy of activation (in eV) for C_2H_2 formation with respect to temperature.

T (K)	Activation barrier for TS-1 (eV)	Activation barrier for TS-2 (eV)	Activation barrier for TS-3 (eV)
DFT	0.56	0.74	0.04
0	0.49	0.67	0.03
298.15	0.45	0.65	0.02
400	0.42	0.63	0.01
600	0.38	0.59	0.00
1000	0.27	0.50	-0.03
1200	0.22	0.46	-0.05

5.5.6 H migration near the vacancy

Table 5.11: Reaction free energy (in eV) and activation energy (in eV) for H diffusion near vacancy with respect to temperature.

T (K)	Diffusion barrier (eV)	Reaction energy (eV)
DFT	1.02	0.09
0	0.98	0.07
298.15	0.92	0.07
400	0.91	0.07
600	0.87	0.07
1000	0.79	0.07
1200	0.76	0.06

5.5.7 H migration on defect-free surface

Table 5.12: Activation energy (in eV) for H diffusion on pristine surface with respect to temperature.

T (K)	Diffusion barrier (eV)
DFT	1.01
0	0.98
298.15	0.93
400	0.91
600	0.87
1000	0.81
1200	0.77

5.5.8 H_2 evolution near the vacancy

Table 5.13: Reaction free energy (in eV) and activation energy (in eV) for H diffusion near vacancy with respect to temperature.

T (K)	Activation barrier TS-1 (eV)	Activation barrier TS-2 (eV)	Reaction energy (eV)
DFT	0.67	0.93	1.50
0	0.61	0.99	1.53
298.15	0.59	0.94	1.53
400	0.59	0.91	1.53
600	0.59	0.85	1.52
1000	0.58	0.73	1.49
1200	0.56	0.67	1.48

5.5.9 Vacancy reoccupation

Table 5.14: Reaction free energy (in eV) and activation energy (in eV) for H_2 evolution at the vacancy after vacancy reoccupation with respect to temperature.

T (K)	Activation barrier TS-1 (eV)	Reaction energy (eV)
DFT	0.54	-0.69
0	0.49	-0.76
298.15	0.46	-0.75
400	0.45	-0.74
600	0.43	-0.72
1000	0.39	-0.68
1200	0.37	-0.67

5.5.10 H_2 evolution at the vacancy after vacancy reoccupation

Table 5.15: Reaction free energy (in eV) and activation energy (in eV) for H_2 evolution at the vacancy after vacancy reoccupation with respect to temperature.

T (K)	Activation barrier TS-1 (eV)	Activation barrier TS-2 (eV)	Reaction energy (eV)
DFT	0.75	0.96	1.61
0	0.77	0.87	1.56
298.15	0.74	0.81	1.55
400	0.73	0.78	1.54
600	0.72	0.70	1.51
1000	0.69	0.55	1.45
1200	0.68	0.47	1.42

Bibliography

(1) Feichter, J.; Schurath, U.; Zellner, R. *Chemie in unserer Zeit* **2007**, *41*, 138–150.

(2) Schwach, P.; Pan, X.; Bao, X. *Chemical Reviews* **2017**, *117*, PMID: 28475304, 8497–8520.

(3) Sun, L.; Wang, Y.; Guan, N.; Li, L. *Energy Technology* **2020**, *8*, 1900826.

(4) Tang, P.; Zhu, Q.; Wu, Z.; Ma, D. *Energy Environ. Sci.* **2014**, *7*, 2580–2591.

(5) Latimer, A.; Kulkarni, A.; Aljama, H.; Montoya, J.; Yoo, J. S.; Tsai, C.; Abild-Pedersen, F.; Studt, F.; Nørskov, J. *Nature materials* **2016**, *16*, DOI: 10.1038/nmat4760.

(6) Zhang, T.; Yang, X.; Ge, Q. *Catalysis Today* **2021**, *368*, Catalytic conversion of low-carbon and sustainable resources, 140–147.

(7) Zhang, T.; Holiharimanana, D.; Yang, X.; Ge, Q. *The Journal of Physical Chemistry C* **2020**, *124*, 26722–26729.

(8) Prats, H.; Gutiérrez, R. A.; Piñero, J. J.; Viñes, F.; Bromley, S. T.; Ramírez, P. J.; Rodriguez, J. A.; Illas, F. *Journal of the American Chemical Society* **2019**, *141*, PMID: 30848129, 5303–5313.

(9) Kuriakose, N.; Mondal, U.; Ghosh, P. *J. Mater. Chem. A* **2021**, *9*, 23703–23713.

(10) Belgued, M.; Amariglio, H.; Pareja, P.; Amariglio, A.; Saint-Just, J. *Catalysis Today* **1992**, *13*, 437–445.

(11) Tan, X.; Tahini, H. A.; Smith, S. C. *The Journal of Physical Chemistry C* **2021**, *125*, 12628–12635.

(12) Guo, X. et al. *Science* **2014**, *344*, 616–619.

(13) Wen, J.-H.; Guo, D.; Wang, G.-C. *Applied Surface Science* **2021**, *555*, 149690.

(14) Kunkel, C.; Viñes, F.; Illas, F. *ACS Applied Energy Materials* **2018**, *1*, 43–47.

(15) Figueras, M.; Gutiérrez, R. A.; Prats, H.; Viñes, F.; Ramírez, P. J.; Illas, F.; Rodriguez, J. A. *Phys. Chem. Chem. Phys.* **2020**, *22*, 7110–7118.

(16) Viñes, F.; Rodriguez, J. A.; Liu, P.; Illas, F. *Journal of Catalysis* **2008**, *260*, 103–112.

(17) Ding, H.; Wang, J.; Li, C.; Nie, J.; Liu, X. *Solid State Communications* **2012**, *152*, 185–188.

(18) Råsander, M.; Hugosson, H. W.; Delin, A. *Journal of Physics: Condensed Matter* **2017**, *30*, 015702.

(19) Wu, S.; Wang, L.; Zhang, J. *Journal of Photochemistry and Photobiology C: Photochemistry Reviews* **2021**, *46*, 100400.

(20) Wen, J.-H.; Wang, G.-C. *The Journal of Physical Chemistry C* **2020**, *124*, 13249–13262.

(21) Li, Z. et al. *Nature Catalysis* **2021**, *4*, DOI: 10.1038/s41929-021-00686-y.

(22) Schobert, H. *Chemical Reviews* **2014**, *114*, PMID: 24256089, 1743–1760.

(23) Martin, R. M., *Electronic Structure: Basic Theory and Practical Methods*; Cambridge University Press: 2004.

(24) Jensen, F., *Introduction to computational chemistry*; John wiley & sons: 2017.

(25) Alavi, S. *Angewandte Chemie International Edition* **2009**, *48*, 9404–9405.

(26) Hohenberg, P.; Kohn, W. *Physical review* **1964**, *136*, B864.

(27) Kohn, W.; Sham, L. J. *Physical review* **1965**, *140*, A1133.

(28) Perdew, J. P.; Burke, K.; Ernzerhof, M. *Phys. Rev. Lett.* **1996**, *77*, 3865–3868.

(29) Payne, M. C.; Teter, M. P.; Allan, D. C.; Arias, T. A.; Joannopoulos, J. D. *Rev. Mod. Phys.* **1992**, *64*, 1045–1097.

(30) Vanderbilt, D. *Physical review B* **1990**, *41*, 7892.

(31) De Vita, A.; Gillan, M. *Journal of Physics: Condensed Matter* **1991**, *3*, 6225.

(32) Giannozzi, P. et al. *Journal of Physics: Condensed Matter* **2009**, *21*, 395502.

(33) Giannozzi, P.; Andreussi, O.; Brumme, T.; Bunau, O.; Nardelli, M. B.; Calandra, M.; Car, R.; Cavazzoni, C.; Ceresoli, D.; Cococcioni, M., et al. *Journal of physics: Condensed matter* **2017**, *29*, 465901.

(34) Perdew, J. P.; Burke, K.; Ernzerhof, M. *Physical review letters* **1996**, *77*, 3865.

(35) Marzari, N.; Vanderbilt, D.; De Vita, A.; Payne, M. *Physical review letters* **1999**, *82*, 3296.

(36) Mao, J.; Li, S.; Zhang, Y.; Chu, X.; Yang, Z. *Applied Surface Science* **2016**, *386*, 202–209.

(37) Baroni, S.; de Gironcoli, S.; Dal Corso, A.; Giannozzi, P. *Rev. Mod. Phys.* **2001**, *73*, 515–562.

(38) Bendavid, L. I.; Carter, E. A. *The Journal of Physical Chemistry C* **2013**, *117*, 26048–26059.

(39) Chase, M. W.; (US), N. I. S. O., *NIST-JANAF thermochemical tables*; American Chemical Society Washington, DC: 1998; Vol. 9.

(40) Manz, T. A.; Limas, N. G. *RSC Adv.* **2016**, *6*, 47771–47801.

(41) Nørskov, J. K.; Studt, F.; Abild-Pedersen, F.; Bligaard, T., *Fundamental concepts in heterogeneous catalysis*; John Wiley & Sons: 2014.

(42) Henkelman, G.; Jónsson, H. *The Journal of Chemical Physics* **2000**, *113*, 9978–9985.

(43) Henkelman, G.; Uberuaga, B. P.; Jónsson, H. *The Journal of Chemical Physics* **2000**, *113*, 9901–9904.

(44) Perdew, J. P.; Burke, K.; Ernzerhof, M. *Phys. Rev. Lett.* **1998**, *80*, 891–891.

(45) Holmblad, P. M.; Larsen, J. H.; Chorkendorff, I. *The Journal of chemical physics* **1996**, *104*, 7289–7295.

(46) Yoshizawa, K.; Suzuki, A.; Yamabe, T. *Journal of the American Chemical Society* **1999**, *121*, 5266–5273.

(47) Pham, T.; Leggesse, E.; Jiang, J. *Catalysis Science & Technology* **2015**, *5*, 4064–4071.

(48) Wu, R.; Tian, F.; Liu, Z.; Xue, X.; Zhang, J.; Zu, J. *Applied Surface Science* **2019**, *481*, 1154–1159.

(49) Viñes, F.; Lykhach, Y.; Staudt, T.; Lorenz, M. P.; Papp, C.; Steinrück, H.-P.; Libuda, J.; Neyman, K. M.; Görling, A. *Chemistry–A European Journal* **2010**, *16*, 6530–6539.

(50) Kozlov, S. M.; Neyman, K. M. *Journal of Catalysis* **2016**, *337*, 111–121.